

The Open University's repository of research publications
and other research outputs

The LOFAR Two-metre Sky Survey (LoTSS) - III. First Data Release: optical/IR identifications and value-added catalogue

Journal Item

How to cite:

Williams, W. L.; Hardcastle, M. J.; Best, P. N.; Sabater, J.; Croston, J. H.; Duncan, K. J.; Shimwell, T. W.; Röttgering, H. J. A.; Nisbet, D.; Gürkan, G.; Alegre, L.; Cochrane, R. K.; Goyal, A.; Hale, C. L.; Jackson, N.; Jamrozy, M.; Kondapally, R.; Kunert-Bajraszewska, M.; Mahatma, V. H.; Mingo, B.; Morabito, L. K.; Prandoni, I.; Roskowinski, C.; Shulevski, A.; Smith, D. J. B.; Tasse, C.; Urquhart, S.; Webster, B.; White, G. J.; Beswick, R. J.; Callingham, J. R.; Chyży, K. T.; de Gasperin, F.; Harwood, J. J.; Hoeft, M.; Iacobelli, M.; McKean, J. P.; Mechev, A. P.; Miley, G. K.; Schwarz, D. J. and van Weeren, R. J. (2019). The LOFAR Two-metre Sky Survey (LoTSS) - III. First Data Release: optical/IR identifications and value-added catalogue. *Astronomy & Astrophysics*, 622, article no. A2.

For guidance on citations see [FAQs](#).

© 2019 ESO



<https://creativecommons.org/licenses/by-nc-nd/4.0/>

Version: Version of Record

Link(s) to article on publisher's website:

<http://dx.doi.org/doi:10.1051/0004-6361/201833564>

oro.open.ac.uk

The LOFAR Two-metre Sky Survey

III. First data release: Optical/infrared identifications and value-added catalogue^{★,★★,★★★}

W. L. Williams¹, M. J. Hardcastle¹, P. N. Best², J. Sabater², J. H. Croston³, K. J. Duncan⁴, T. W. Shimwell^{5,4}, H. J. A. Röttgering⁴, D. Nisbet², G. Gürkan⁶, L. Alegre², R. K. Cochrane², A. Goyal⁷, C. L. Hale⁸, N. Jackson⁹, M. Jamrozy⁷, R. Kondapally², M. Kunert-Bajraszewska¹⁰, V. H. Mahatma¹, B. Mingo³, L. K. Morabito⁸, I. Prandoni¹¹, C. Roskowinski¹⁰, A. Shulevski¹², D. J. B. Smith¹, C. Tasse^{13,14}, S. Urquhart³, B. Webster³, G. J. White^{3,15}, R. J. Beswick⁹, J. R. Callingham⁵, K. T. Chyży⁷, F. de Gasperin¹⁶, J. J. Harwood¹, M. Hoeft¹⁷, M. Iacobelli⁵, J. P. McKean^{5,18}, A. P. Mechev⁴, G. K. Miley⁴, D. J. Schwarz¹⁹, and R. J. van Weeren⁴

(Affiliations can be found after the references)

Received 4 June 2018 / Accepted 9 November 2018

ABSTRACT

The LOFAR Two-metre Sky Survey (LoTSS) is an ongoing sensitive, high-resolution 120–168 MHz survey of the northern sky with diverse and ambitious science goals. Many of the scientific objectives of LoTSS rely upon, or are enhanced by, the association or separation of the sometimes incorrectly catalogued radio components into distinct radio sources and the identification and characterisation of the optical counterparts to these sources. We present the source associations and optical and/or IR identifications for sources in the first data release, which are made using a combination of statistical techniques and visual association and identification. We document in detail the colour- and magnitude-dependent likelihood ratio method used for statistical identification as well as the Zooniverse project, called LOFAR Galaxy Zoo, used for visual classification. We describe the process used to select which of these two different methods is most appropriate for each LoTSS source. The final LoTSS-DR1-IDs value-added catalogue presented contains 318 520 radio sources, of which 231 716 (73%) have optical and/or IR identifications in Pan-STARRS and WISE.

Key words. surveys – catalogues – radio continuum: general

1. Introduction

The true power of modern large radio surveys, which will reveal many millions of radio sources, lies in cross-matching them with surveys at different wavelengths, i.e. in identifying the multiwavelength counterparts of radio sources. This enables detailed statistical studies of the populations of extragalactic radio sources and their host galaxy properties. Over the last few decades, the cross-matching of large area radio surveys, in particular the National Radio Astronomy Observatory (NRAO) Very Large Array (VLA) Sky Survey (NVSS; Condon et al. 1998) and the Faint Images of the Radio Sky at Twenty centimetres (FIRST) survey (Becker et al. 1995), with large-scale optical spectroscopic surveys, such as the Sloan Digital Sky Survey (SDSS; York et al. 2000; Stoughton et al. 2002) and the 6 degree Field Galaxy Survey (6dFGS; Jones et al. 2004), have hugely improved our understanding of extragalactic radio sources. Matching these surveys has provided samples of many thousands of sources (e.g. Best et al. 2005a; Mauch & Sadler 2007), which have allowed for detailed statistical studies of the radio source populations (e.g. Best et al. 2005b; Best & Heckman 2012; Janssen et al. 2012).

In the coming years, a number of wide area surveys will be carried out using the next generation of radio telescopes and telescope upgrades. These include the LOw Frequency ARray (LOFAR; van Haarlem et al. 2013) Two-metre Sky Survey (LoTSS; Shimwell et al. 2017), the VLA Sky Survey (VLASS¹), the Evolutionary Map of the Universe survey (EMU; Norris et al. 2011) using the Australian SKA Pathfinder (ASKAP; Johnston et al. 2007), and the WODAN survey (Röttgering et al. 2011) using the APERTure Tile In Focus (APERTIF; Verheijen et al. 2008) upgrade on the Westerbork Synthesis Radio Telescope (WSRT). New large-area optical surveys are also in progress or planned. These include surveys with the Panoramic Survey Telescope and Rapid Response System (Pan-STARRS; Kaiser et al. 2002, 2010), the Large Synoptic Survey Telescope (LSST; Ivezić et al. 2008) and *Euclid* (Amendola et al. 2018). Deep X-ray surveys with eROSITA are also planned (Merloni et al. 2012). When combined, these next generation radio and multiwavelength surveys will provide samples orders of magnitude larger than currently available, reaching to substantially higher redshifts, which will revolutionise our understanding of radio source populations through far more detailed statistical studies.

Cross-matching surveys at different wavelengths is a well-established procedure in astronomy, albeit with some unresolved challenges. For many radio sources, including star-forming galaxies and some radio-loud active galactic nuclei (AGN), the

[★] LoTSS.

^{★★} The value-added catalogue is available online at <https://lofar-surveys.org/>, as part of this data release.

^{★★★} The catalogue is only available at the CDS via anonymous ftp to cdsarc.u-strasbg.fr (130.79.128.5) or via <http://cdsarc.u-strasbg.fr/vizbin/qcat?J/A+A/622/A1>

¹ <https://science.nrao.edu/science/surveys/vlass>

radio emission is relatively compact and is coincident with the optical emission, allowing cross-matching through simple procedures, such as nearest neighbour (NN) matching or more complex automated statistical methods. However, problems of matching between the radio and optical are compounded by the complex nature of other radio sources, in particular spatially extended radio-loud AGN: these scientifically interesting complex-structured sources are very challenging to cross-match.

A sensitive, high-resolution 120–168 MHz survey of the northern sky, LoTSS, is already well under way. Using the High Band Antenna (HBA) system of LOFAR, the survey aims to reach a sensitivity of less than $0.1 \text{ mJy beam}^{-1}$ at an angular resolution of $\sim 6''$ across the whole northern hemisphere. The first data release (LoTSS-DR1), described in the accompanying paper (Shimwell et al. 2019; hereafter DR1-I), covers 424 square degrees and includes over 300 000 radio sources. While surveys like NVSS lack angular resolution and surveys like FIRST have problems with resolving out large-scale emission, LoTSS is unique in retaining both high resolution and sensitivity to large-scale structures, which aids the process of cross-matching. Many of the scientific objectives of LoTSS rely upon, or are enhanced by, the identification and characterisation of the multiwavelength counterparts to the detected radio sources. In this paper we have made our first attempt at enriching our radio catalogues by identifying their optical/IR² counterparts, thereby enabling their photometric and spectroscopic redshifts to be determined. Accurate source redshifts allow physical properties such as luminosities and sizes to be determined, which in turn enables studies of the intrinsic properties of radio sources and their host galaxies³. Photometric redshift and rest-frame colour estimates for all the matched optical/IR sources are presented in the accompanying paper (Duncan et al. 2019; hereafter DR1-III). Furthermore, future spectroscopic surveys such as WEAVE-LOFAR (Smith et al. 2016), using the *William Herschel* Telescope Enhanced Area Velocity Explorer (WEAVE; Dalton et al. 2012, 2014) multi-object and integral field spectrograph, will provide precise redshift estimates and robust source classification for large fractions of the LoTSS source population.

This paper is structured as follows. In Sect. 2 we give a brief summary of the LoTSS and optical/IR data used for the cross-matching. In Sect. 3 we give an overview of the process of radio–optical cross-matching. The details of the statistical likelihood ratio (LR) technique are given in Sect. 4 and the full Zooniverse visual classification scheme is described in Sect. 5. In Sect. 6 we present the decision tree that is used to decide which sources are identified by the likelihood ratio and visual classification methods. The final value-added catalogue is presented in Sect. 7, along with some of its basic properties. Finally, we summarise our work and discuss some possible future developments in Sect. 8.

Throughout this paper, all magnitudes are quoted in the AB system (Oke & Gunn 1983) unless otherwise stated.

2. The radio and optical catalogues

2.1. The LOFAR sample

Details of the LoTSS first data release images and source extraction are given in DR1-I and we summarise the relevant points.

² In this paper we take optical/IR to mean the inclusive or, i.e. optical or IR or both.

³ For examples of the broad range of science see the other papers in this special issue.

The images cover 424 square degrees over⁴ the *Hobby-Eberly Telescope Dark Energy Experiment* (HETDEX; Hill et al. 2008) Spring Field (RA $10^{\text{h}}45^{\text{m}}\text{--}15^{\text{h}}30^{\text{m}}$ and Dec $45^{\circ}00'\text{--}57^{\circ}00'$). Direction-dependent calibration of the LOFAR data enabled imaging at the full resolution of $6''$. Source detection was performed on each mosaic image using the PYTHON Blob Detector and Source Finder (PyBDSF; Mohan & Rafferty 2015). The background noise was estimated across the images using sliding box sizes of 30×30 synthesised beams, decreased to just 12×12 synthesised beams near high signal-to-noise (S/N) sources (≥ 150) to more accurately capture the increase in noise over smaller spatial scales in these regions. Wavelet decomposition, with 4 wavelet scales, was used to better characterise the complex extended emission present in the images. We set PyBDSF to form islands with a 5σ peak detection threshold and a 4σ island threshold. Internally PyBDSF fitted each island with one or more Gaussians that were grouped into discrete sources. The parameters we used for the source extraction (namely the box sizes for determining the background noise and the “group_tol” parameter, for which we used a value of 10) were optimised through trial and error testing⁵. This allowed us to produce the best grouping of Gaussian components, i.e. to join up most compact double sources while not overproducing “blended” sources (incorrectly grouping separate sources as one source). Sources fitted with multiple Gaussians are identified in the PyBDSF source catalogue by a value of “M” in the “S_Code” column, those fitted by a single Gaussian have “S” in the “S_Code” column, and a few tens of sources that are fitted by a single Gaussian, but lie within the same island as another source, have “C” in the “S_Code” column. We treat “C” type sources the same as “M” type sources.

A final PyBDSF source catalogue of the HETDEX region, containing 325 694 entries, was produced, along with a final catalogue of all the Gaussian components of the PyBDSF sources. In the following we refer to the source catalogue as the PyBDSF source catalogue and the Gaussian component catalogue as the PyBDSF Gaussian catalogue. Catalogue parameters refer to those from the PyBDSF source catalogue, unless explicitly specified as the parameters from the PyBDSF Gaussian component catalogue. DR1-I determined the positional accuracy of the catalogued sources to be within $0.2''$.

2.2. The optical/infrared galaxy sample

Deep and wide optical and IR data are available over the LoTSS-DR1 sky area from Pan-STARRS (in *grizy* bands) and from the Wide-field Infrared Survey Explorer (WISE; Wright et al. 2010). The Pan-STARRS 3π survey (Chambers et al. 2016) covers the entire sky north of $\delta > -30^\circ$ with 5σ magnitude limits in the stacked *grizy* images of 23.3, 23.2, 23.1, 22.3 and 21.4 mag, respectively. The typical point spread function (PSF) of the Pan-STARRS images is $\sim 1\text{--}1.3''$. The AllWISE catalogue (Cutri et al. 2013) includes photometry in the 3.4, 4.6, 12, and $22 \mu\text{m}$ mid-infrared bands (W1, W2, W3, and W4) for more than 747 million sources over the full sky. The W1 and W2 bands have significantly better sensitivity than the other two WISE bands; the AllWISE catalogue completeness varies over the sky, but nominally it is $> 95\%$ complete for sources with $W1 < 19.8$, $W2 < 19.0$, $W3 < 16.67$, and $W4 < 14.32$ mag. The effective PSF for

⁴ LoTSS-DR1 covers a region slightly larger than the HETDEX field, but with a few holes from four failed LOFAR pointings.

⁵ This was done by visually examining the output catalogues overlaid on the LoTSS images prior to any of the visual classification presented in this paper.

the WISE images is 6–6.5'' in bands W1, W2, and W3, and ~12'' in W4.

We produced a combined Pan-STARRS–AllWISE catalogue over the LoTSS coverage area by matching sources in the two catalogues using the LR method, the details of which are given in Sect. 4.2.1. This combined catalogue includes sources with detections in only PanSTARRS or only AllWISE or both and is used for identifying the optical/near-infrared counterparts to LoTSS sources and in the determination of photometric redshifts and rest-frame colours (DR1-III).

For some large optical galaxies we make use of other earlier all-sky surveys, in particular, we use the SDSS DR-12 catalogue (Alam et al. 2015) and the Two Micron All Sky Survey (2MASS; Skrutskie et al. 2006) extended source catalogue (2MASX; Jarrett et al. 2000). We refer only to source names in these catalogues.

3. Radio-optical cross-matching

Our objectives throughout this paper are essentially to correctly “associate” radio sources – that is, to decide which sources found by the source finder belong together as components of one physical source and which are separate sources that have been incorrectly associated by the source finder – and to “identify” them – that is, to find the best possible optical/IR counterpart where one exists.

The PyBDSF catalogue is not a perfect representation of radio sources. In addition to the unambiguous complete sources, this catalogue contains a mixture of (i) blended sources, where distinct nearby sources have been incorrectly associated as one source; (ii) separate components of distinct sources, where a single source has been catalogued in multiple entries because there is no contiguous emission between its components (for example in the case of separate lobes of radio galaxies) so that the true association is not recovered by the source finder; and (iii) spurious emission or artefacts. We aim to produce a catalogue of real, correctly associated radio sources and to provide their Pan-STARRS/WISE counterparts, where possible. We handle the counterpart identification and possible association or separation of incorrectly catalogued components in two ways; we use a separate decision process to determine which of the two methods to use based on the properties of the radio sources.

The first method determines the presence or absence of a counterpart statistically. For this we use the LR, i.e. the ratio of the probability of a particular source being the true counterpart to that of it being a random interloper. This method is described in detail in Sect. 4, and the specific application to this data set is described in Sect. 4.2. Initially we determine the LR counterparts for all sources in the PyBDSF catalogue with sizes smaller than 30'' as well as for all the PyBDSF Gaussian components smaller than 30''. These can be incorrectly combined into sources by PyBDSF and individually have superior LR matches by themselves; for sources and Gaussian components larger than 30'' we do not attempt to find LR matches as the size of these sources or components make the LR identification unreliable.

For larger and more complex sources, statistical matching is not reliable so we employ a second method for identification and association or separation of components. This method involves human visual classification and is built on a Zooniverse framework. The project, called LOFAR Galaxy Zoo (LGZ), is described in detail in Sect. 5. Since it is prohibitive in terms of time, as well as unnecessary, to do this for all sources in the PyBDSF catalogue, we preselect for LGZ processing samples of sources that are likely to be complex.

The sources in the PyBDSF catalogue are selected either for LGZ processing or for acceptance of the LR match based on their catalogued characteristics by means of a decision tree described Sect. 6. The main PyBDSF catalogue parameters we use for the decisions are the source size (defined as the major axis), the source flux density, the number of fitted Gaussian components, the distance to the NN, and the distance to the fourth closest neighbour. In the decision tree we further make use of the LRs determined for all sources in the catalogue smaller than 30'', as well as the LRs for all the Gaussian components smaller than 30''. The thresholds used to determine whether a given source or Gaussian component has an acceptable LR match are discussed in Sect. 4.

4. Likelihood ratio identifications

In this section we describe the statistical LR method and how it is used to identify the majority of sources in the LoTSS-DR1 catalogue. The general description of the method is given in Sect. 4.1 and the specific application to the LoTSS-DR1 data set in Sect. 4.2. As discussed in Sect. 2, deep and wide area data for host galaxy identifications are available over the LoTSS-DR1 sky area from Pan-STARRS and AllWISE. We use a magnitude-only LR method to cross-match the Pan-STARRS and AllWISE catalogues over the LoTSS-DR1 sky coverage and produce a combined Pan-STARRS and AllWISE catalogue, which includes sources with detections in only PanSTARRS or only AllWISE or both (see Sect. 4.2.1 for details), and thus includes colour information for each source. The LoTSS-DR1 sources are cross-matched with this combined Pan-STARRS–WISE catalogue using a colour- and magnitude-dependent LR method (see Sect. 4.2.2 for details).

4.1. The likelihood ratio method

The LR technique (e.g. Richter 1975; de Ruiter et al. 1977; Sutherland & Saunders 1992) is a maximum likelihood method used to statistically investigate whether an object observed at one wavelength is the correct counterpart of an object observed at a different wavelength. It is particularly useful when the basis catalogue has a poorer angular resolution or lower source density than the catalogue in which the counterpart is being sought, thus giving rise to multiple potential matches from which the most likely counterpart needs to be identified. This is often the case when seeking optical or IR identifications to radio sources, as in this paper. In the description below we specifically use “radio” to refer to the basis catalogue and “optical” to refer to the catalogue being matched to. However, these terms can be more generally replaced by any basis catalogue and matched catalogue – for example, we also use the LR technique to find Pan-STARRS counterparts to AllWISE sources.

The LR of an object is defined as the ratio of the probability of the object being the true counterpart to that of it being a random interloper. This can be generally written as

$$LR = \frac{q(x_1, x_2, \dots)f(r)}{n(x_1, x_2, \dots)} \quad (1)$$

Here, $q(x_1, x_2, \dots)$ represents the a priori probability that the radio source has a counterpart with parameters (which might be any magnitudes, colours, redshift, type, or any other galaxy property to be included in the analysis) with values x_1, x_2 , etc. The parameter $n(x_1, x_2, \dots)$ is the sky surface density of objects with properties x_1, x_2 , etc.; $f(r)$ is the probability distribution function for the offset r between the position of the radio source

and its potential counterpart, taking into account the uncertainties in the positions of each.

Likelihood ratios are commonly calculated using a single galaxy magnitude (m) as the only parameter, in which case

$$\text{LR} = \frac{q(m)f(r)}{n(m)}. \quad (2)$$

We use this simple approach for cross-matching the PanSTARRS and WISE catalogues. The methods for determination of $f(r)$, $n(m)$, and $q(m)$ are discussed below.

Nisbet (2018) showed, using an analysis of LOFAR sources in the ELAIS-N1 field, that including galaxy colour (in their case, $g - i$ and $i - K$ colours) as well as magnitude greatly increased the robustness of the LR analysis for radio source host galaxies. The inclusion of the $i - K$ colour was particularly useful, as radio source hosts are well known to be frequently red in optical to near-IR colours: galaxies of given i -band magnitude were found to be around an order of magnitude more likely to host a radio source if they had a colour $i - K > 4$ than those with $i - K < 3$. In the LR analysis for the LoTSS sources we therefore consider magnitude and colour (c), and use

$$\text{LR} = \frac{q(m, c)f(r)}{n(m, c)}. \quad (3)$$

Specifically, we use the Pan-STARRS i -band data and the WISE W1 ($3.4\mu\text{m}$) data, as these offer the highest detection fractions for the radio sources and also provide an optical-to-IR colour baseline similar to the $i - K$ colour used by Nisbet (2018).

4.1.1. Determination of $f(r)$

The parameter $f(r)$ represents the probability distribution of offset r between the catalogued positions of the radio source and its potential counterpart. The uncertainty in this offset is calculated by combining the uncertainty on the radio position, the uncertainty on the optical/IR position, and the uncertainty on the relative astrometry of the two surveys. It is important to take into account that radio positional errors are frequently asymmetric due to an elliptical beam shape, or an extended radio source. Therefore we need to evaluate radio-optical offsets relative to the major and minor axis direction of each source (as opposed to working in the RA and Dec directions, which are in general not aligned with the PSF), as well as along the direction between the radio source and possible counterpart. The parameter $f(r)$ is then given by

$$f(r) = \frac{1}{2\pi\sigma_{\text{maj}}\sigma_{\text{min}}} \exp\left(\frac{-r^2}{2\sigma_{\text{dir}}^2}\right), \quad (4)$$

where σ_{maj} and σ_{min} are the combined positional uncertainties along the radio source major and minor axis directions, and σ_{dir} is the combined positional uncertainty projected along the direction from the radio source to the possible counterpart under investigation. We now discuss each component of the positional error budget in turn.

For each LoTSS source, PyBDSF returns the error on the full width at half maximum (FWHM) of the major and minor axes for the fitted Gaussian ($\delta_{\text{FWHM}, \text{maj}}$, $\delta_{\text{FWHM}, \text{min}}$) as well as the position angle. As shown by Condon (1997), the uncertainty on the radio position along the major (minor) axis direction ($\sigma_{\text{maj}(\text{min}), \text{rad}}$) is formally given by $\sigma_{\text{maj}(\text{min}), \text{rad}} = \delta_{\text{FWHM}, \text{maj}(\text{min})}/(8 \ln 2)^{1/2}$. However, this does not take into account the presence of correlated noise in the radio images;

empirical results from the NVSS (Condon et al. 1998) and WENSS (Rengelink et al. 1997) surveys indicate that the formal positional errors on the radio sources are typically a factor of 1.3–1.5 larger. Here, a factor $\sqrt{2}$ is adopted, and so the positional uncertainties along the major and minor axes are $\sigma_{\text{maj}(\text{min}), \text{rad}} = \delta_{\text{FWHM}, \text{maj}(\text{min})}/(4 \ln 2)^{1/2}$. Then, using the angle between the major axis direction and that of the vector joining the LoTSS source to its potential counterpart, these two uncertainties are projected to derive the radio positional uncertainty in the direction of the potential counterpart ($\sigma_{\text{dir}, \text{rad}}$).

The positional uncertainties for the optical/IR galaxy are catalogued in the RA and Dec directions; these are therefore re-projected into the radio source major axis, minor axis, and source-to-counterpart directions ($\sigma_{\text{maj}, \text{opt}}$, $\sigma_{\text{min}, \text{opt}}$ and $\sigma_{\text{dir}, \text{opt}}$), although in practice these uncertainties are often symmetric. For the astrometric uncertainty between the radio and counterpart surveys, a value of $\sigma_{\text{ast}} = 0.6''$ is adopted. This is larger than the typical astrometric uncertainty determined by DRI-I but, as discussed in Nisbet (2018), it is important to take a conservative approach as the astrometric errors are generally not Gaussian. For most sources, the astrometric uncertainty makes a negligible contribution to the overall uncertainty, but adoption of too small a value can lead to a failure to select genuine counterparts for some bright compact radio sources for which S/N dependent positional uncertainties can be unrealistically small. The value of $\sigma_{\text{ast}} = 0.6''$ was chosen empirically by visually examining borderline cases of bright compact radio sources.

These three contributions are combined in quadrature to derive the overall positional uncertainty required in Eq. (4), i.e.

$$\sigma_{\text{maj}}^2 = \sigma_{\text{maj}, \text{rad}}^2 + \sigma_{\text{maj}, \text{opt}}^2 + \sigma_{\text{ast}}^2 \quad (5)$$

and similarly for σ_{min} and σ_{dir} . Thus, $f(r)$ can be calculated for each potential counterpart.

4.1.2. Determination of $n(m)$ and $n(m, c)$

The parameter $n(m)$ represents the number of objects per unit area of sky at a given magnitude, and is easily calculated using a well-defined, representative large region of sky, which is not significantly affected by bright stars or other limitations that cause incompleteness in the survey. A Gaussian kernel density estimator (KDE) of width 0.5 mag was used to determine $n(m)$; particularly for the smaller number statistics of $q(m)$ at bluer colours (see Sect. 4.2.2), a KDE provides smoother and more robust results than binning.

In colour space, to determine $n(m, c)$, the sample is divided into colour bins and $n(m)$ is determined separately for galaxies within each colour bin. Adoption of a two-dimensional KDE in both colour and magnitude was considered, but would have required highly adaptive scaling lengths to account for both the broad colour tails and the rapid changes in $q(m)/n(m)$ at intermediate colours.

4.1.3. Determination of $q(m)$

The parameter $q(m)$ represents the a priori probability that the radio source has a counterpart of magnitude m . Ideally this would be predetermined using an independent data set. However, in general this is not possible and the data set itself must be used; great care must be taken to avoid biases due to galaxy clustering.

Methods to estimate $q(m)$ have been developed by Ciliegi et al. (2003), Fleuren et al. (2012), and McAlpine et al. (2012), amongst others. By defining a fixed search radius r_{max}

(typically chosen to be comparable to the angular resolution of the basis survey), the magnitude distribution of all optical/IR sources within r_{\max} of all the radio sources can be determined (usually referred to as $\text{total}(m)$). This can be statistically corrected for background galaxy counts to determine the magnitude distribution of just the galaxy counts associated with the radio sources ($\text{real}(m)$) using

$$\text{real}(m) = \text{total}(m) - n(m)N_{\text{radio}}\pi r_{\max}^2, \quad (6)$$

where N_{radio} is the number of radio sources in the catalogue (and hence the second term accounts for the total sky area out to r_{\max} around all N_{radio} sources). Determined in this way, $\text{real}(m)$ contains the true radio source host galaxies, but may also include additional galaxies within r_{\max} around the radio sources that are not themselves the host, but are associated with it (e.g. because radio-loud AGN often lie in overdense group or cluster environments, e.g. [Prestage & Peacock 1988](#); [Hill & Lilly 1991](#); [Best 2004](#)). This issue will be returned to shortly.

The parameter $q(m)$ is then derived from $\text{real}(m)$ as

$$q(m) = \frac{\text{real}(m)}{\sum_{m_i} \text{real}(m_i)} Q_0, \quad (7)$$

where Q_0 represents the fraction of sources that have a counterpart down to the magnitude limit of the survey (i.e. $Q_0 = N_{\text{matched}}/N_{\text{radio}}$). [Fleuren et al. \(2012\)](#) outlined a method to derive Q_0 in a manner unbiased by galaxy clustering by comparing the number of the fields around the radio sources which are blank (i.e. without any possible counterparts) out to a chosen search radius⁶ r_s , (referred to as $N_{\text{blank}}(r_s)$) to the number of blanks around an equivalent number of randomly chosen positions ($N_{\text{blank,ran}}(r_s)$),

$$F(r_s)Q_0 = 1 - \frac{N_{\text{blank}}(r_s)}{N_{\text{blank,ran}}(r_s)}, \quad (8)$$

where $F(r_s)$ is the fraction of the true identifications that are expected to be found within radius r_s . Formally $F(r_s)$ should be derived by integrating $f(r)$ for each source, across all position angles, out to r_s , but in practice it is accurate enough to take an average value of σ , in which case $F(r_s) = 1 - \exp(-r_s^2/2\sigma^2)$.

Derived in this way, Q_0 is unbiased by the effects of galaxy clustering; this is because the calculation relies on counting blank fields, so is unaffected by whether a detected radio source host galaxy also has associated companion galaxies within the search radius. However, as noted above, the magnitude distribution $q(m)$ may still be mildly affected by the companion objects.

4.1.4. Determination of $q(m, c)$

This same method cannot easily be adopted across different colour bins. Although $\text{real}(m, c)$ can be easily determined in each colour bin using Eq. (6), the [Fleuren et al. \(2012\)](#) method of Eq. (8) is not able to correct for clustering biases in the determination of $Q_0(c)$ (the fraction of sources with a counterpart of colour c , such that $Q_0(c) = N_{\text{matched}}(c)/N_{\text{radio}}$ and $\sum_c Q_0(c) = Q_0$). This can be seen by considering the case of a radio source host in one colour bin which has a physically associated companion galaxy (i.e. a companion galaxy within the same group or cluster) within the search radius, but which falls in a different colour bin. In this case, as well as (correctly) not being a blank field in the colour bin of the true

host galaxy, that radio source would also not be a blank field when examining the colour bin corresponding to the companion galaxy. Since the companion galaxy is not a random interloper, the search around random positions ($N_{\text{blank,ran}}(r_s)$) would not correct for this. Hence, this radio source would contribute towards $Q_0(c)$ in the colour bins of both the true host galaxy and the companion, leading to an overestimate of Q_0 by as much as tens of percent for larger values of r_s .

Instead, therefore, we adopt the process developed by [Nisbet \(2018\)](#), which is to derive $q(m, c)$ through an iterative approach. Our specific adaptation of this is outlined in more detail in Sect. 4.2.2, but in summary the iterative approach works as follows:

1. First, a rough starting estimate is made for the set of host galaxies to the radio sources. In principle, this starting estimate could be as simple as a NN cross-match out to some fixed radius. In practice, in order to speed up the convergence of the iterative procedure, we produce this starting estimate by using magnitude-only LR analyses in the Pan-STARRS i -band and WISE W1 bands (see Sect. 4.2.2 for the specific details of how we do this).
2. This first-pass list of host galaxies is then split by colour to provide a direct estimate of each of the $Q_0(c)$ – the fraction of radio sources which have counterparts within each colour bin. Dividing by magnitude as well then gives a first estimate of $q(m, c)$ – the fraction of radio sources with a counterpart of magnitude m and colour c .
3. Using this $q(m, c)$ estimate, LR are derived for all galaxies around the radio sources (out to some radius – in our case $15''$) using both magnitude and colour parameters.
4. Using these LR values, a revised estimate for the list of host galaxies is produced by selecting the highest LR match to each radio source, provided that it exceeds the LR threshold (see Sect. 4.1.5).
5. This revised set of matches is used to provide improved estimates of $Q_0(c)$ and $q(m, c)$, and steps 3–5 are iterated to convergence.

4.1.5. Likelihood ratio thresholds

Once all three probability distributions ($f(r)$, $n(m)$ and $q(m)$, or $n(m, c)$ and $q(m, c)$) are determined, Eqs. (2) or (3) (as appropriate) can be used to determine the LR of each candidate host galaxy. The remaining issue is then to decide which identifications to adopt. An advantage of the LR technique is that, in ambiguous cases, multiple possible host galaxy identifications can be retained, with a probability of association assigned to each. However, for this first LoTSS data release, we retain only the most likely match (i.e. the object with the highest LR), if its LR is above our defined threshold level.

For a given LR threshold L_{thr} , the completeness ($C(L_{\text{thr}})$: the fraction of real identifications which are accepted) and the reliability ($R(L_{\text{thr}})$: the fraction of accepted identifications which are correct)⁷ of the resultant sample can be determined as (e.g. [de Ruiter et al. 1977](#); [Best et al. 2003](#))

$$C(L_{\text{thr}}) = 1 - \frac{1}{Q_0 N_{\text{radio}}} \sum_{\text{LR}_i < L_{\text{thr}}} \frac{Q_0 \text{LR}_i}{Q_0 \text{LR}_i + (1 - Q_0)}, \quad (9)$$

$$R(L_{\text{thr}}) = 1 - \frac{1}{Q_0 N_{\text{radio}}} \sum_{\text{LR}_i \geq L_{\text{thr}}} \frac{1 - Q_0}{Q_0 \text{LR}_i + (1 - Q_0)}, \quad (10)$$

⁶ In theory the resultant Q_0 should be insensitive to the radius chosen. In practice, Q_0 is usually evaluated for a range of radii around the angular resolution of the basis catalogue, and an average value taken.

⁷ We note that defining the reliability in this sense – referring to the whole catalogue – is distinct from the reliability as used in the LR formalism by for example [Sutherland & Saunders \(1992\)](#).

where the summation for the completeness calculation is over the highest LR counterparts to all sources for which the best match has a LR below the threshold, and the summation for the reliability is for the best matches above the threshold. The choice of L_{thr} then depends on the relative importance of completeness and reliability for the sample under investigation, but a typical value might be where these two functions cross, or where their average is maximised. We note that the point where completeness and reliability cross is also the value of L_{thr} which delivers a fraction Q_0 of identifications. This is the threshold adopted for the current analysis.

4.2. Practical application to the LoTSS data set

4.2.1. Combining Pan-STARRS and WISE data

Before combining with the radio data, the Pan-STARRS *i*-band and WISE *W1*-band data sets were first combined, using a magnitude-only LR analysis. The WISE *W1* was used as the basis data set and the best Pan-STARRS match (if any) to each WISE source was sought. The matching was done in this direction, since both the angular resolution and source density of the Pan-STARRS data are much higher, and so matching in the opposite direction would lead to multiple Pan-STARRS galaxies selecting the same WISE source. The use of WISE data helps the subsequent LR matching to LoTSS sources given that radio sources are frequently associated with galaxies with redder colours and hence brighter near-infrared magnitudes. Although we do not explicitly filter out optical galaxies with no WISE emission, our colour-based LR method is effective at rejecting these when they are unrelated.

Prior to matching, for the small fraction (<5%) of Pan-STARRS sources without a measured *i*-band magnitude, the *i*-band magnitude was estimated from the measurements in the other Pan-STARRS bands (*grzy*) and the mean colours of the all galaxies; this was done by extracting the magnitude in each band in which the source was detected, adjusting this by the mean colour of all galaxies between that band and the *i*-band, and then averaging these values.

Then, using the techniques described above for magnitude-only LR (Sect. 4.1) and using the AllWISE catalogue as the basis catalogue, an LR threshold of $L_{\text{thr}} = 6.4$ and a value of $Q_0 = 0.62$ were derived (i.e. 62% of WISE *W1* sources have a counterpart in the Pan-STARRS *i*-band data). Likelihood ratios were then derived for all PanSTARRS sources within 15'' of each AllWISE position, and for each AllWISE source the highest LR above the threshold (if any) was taken as the PanSTARRS counterpart. The counterparts accepted (those with $\text{LR} > 6.4$) are broadly similar to those that would be selected by adopting a simple NN radial cross-matching out to $\approx 2''$, but with a weak magnitude dependence on the allowable radial offset.

A combined Pan-STARRS–WISE catalogue was constructed by including all accepted cross-matches, but also retaining all WISE sources without a Pan-STARRS match, and supplementing the catalogue with all of the Pan-STARRS catalogue sources that had not been matched to a WISE source. For all catalogue entries, the magnitudes were converted into AB magnitudes and corrected for Galactic reddening using the data of Schlegel et al. (1998). The overall catalogue contains around 26.5 million entries, of which just over 30% had detections in both bands, nearly 20% were detected only in WISE, and 50% were detected by Pan-STARRS only. Some issues will undoubtedly remain with the combined catalogue, for example in cases where two nearby Pan-STARRS sources are blended in the lower resolution WISE data into a single catalogue entry; however,

these are sufficiently rare that they are not expected to have a significant effect on subsequent LoTSS cross-matching. We note that no attempt was made to separate stars from galaxies in the combined catalogue: LoTSS sources may match to stellar objects (either genuine – such as Pulsars – or misclassified objects such as quasars) and the adopted colour-dependent procedure already works sufficiently well at down-weighting the LRs of stellar candidates that attempting to exclude these would introduce more errors or biases than potential benefit.

4.2.2. Combining LoTSS and Pan-STARRS–WISE data

We use the full colour- and magnitude-dependent LR method described in Sect. 4.1 to cross-match the LoTSS-DR1 sources with the combined Pan-STARRS–WISE catalogue. Specifically, in the LR analysis we consider the *i*-band magnitude (*m*) and the *i* – *W1* colour (*c*). For the 80% of sources with detections in Pan-STARRS, we use the Pan-STARRS positions, while for the remainder we use the WISE positions.

From within the overall LoTSS-DR1 sample, the subset of radio sources for which LR analysis is appropriate was selected. These are ideally the sources for which the PyBDSF radio source position provides a well-defined location for where the radio source host galaxy is expected to be, and not those PyBDSF sources that are parts of a larger source or are very significantly extended and thus have poorly defined positions. Initially, for this sample we included all LoTSS sources smaller than 30''. This initial sample was used to calibrate the $q(m, c)$ values and calculate the LRs as described in this section, noting that these values and LRs are slightly biased by the inclusion of some sources for which LR analysis is not appropriate. The full decision tree, using the LRs as described in Sect. 6, was then used to reselect the sample of LoTSS sources for which LR analysis is appropriate. We also excluded any PyBDSF source already associated in LGZ. This cleaner sample was later used to recalibrate the $q(m, c)$ values, recalculate the LRs, and hence derive the cross-matched counterparts.

As a starting point for the iterative procedure to derive $q(m, c)$ described above (Sect. 4.1.4), an initial pass of determining optical/IR counterparts is required. This was achieved by cross-matching the radio sources selected for LR analysis against the *i*-band and *W1*-band catalogues separately, in each case using a LR analysis considering magnitude only. Specifically, for this magnitude-only matching, first the Fleuren et al. (2012) technique was used to derive values of $Q_{0,i} = 0.512$ and $Q_{0,W1} = 0.700$ (i.e. 51% and 70% identification rates for LoTSS sources in the *i* and *W1* bands, respectively) and the corresponding $q(m)$ distributions. Then, the LRs were then derived for all sources in each of the *i*-band and *W1*-band catalogues located within 15'' of each radio position. Sources were accepted as matches if their LRs were above the thresholds of $L_{\text{thr}} = 4.85$ in the *i*-band or $L_{\text{thr}} = 0.70$ in the *W1*-band (corresponding to a fraction of Q_0 accepted matches in each band; see Sect. 4.1.5). If more than one potential counterpart was above those thresholds then the counterpart with the highest LR in either of the two bands was accepted and the other discarded. Creating the starting sample in this manner, rather than a simple cross-match or a LR analysis in one band alone, produced a more accurate starting estimate for $q(m, c)$ and led to faster convergence of the iterative procedure.

The sources in the combined Pan-STARRS–WISE catalogue were then divided into 16 colour bins. Two colour bins corresponded to those objects detected only in the *i*-band and only in the *W1*-band. A further 14 colour categories were defined

Table 1. Colour bins adopted for LR analysis.

Colour bin	$f_{\text{PS-WISE}}$	$Q_0(c)$	N_{LoTSS}	f_{radio}
$i - W1 \leq 0$	0.034	0.0010	299	0.001
$0 < i - W1 \leq 0.5$	0.024	0.0056	1675	0.006
$0.5 < i - W1 \leq 1.0$	0.036	0.0251	6878	0.019
$1.0 < i - W1 \leq 1.25$	0.026	0.0359	9459	0.037
$1.25 < i - W1 \leq 1.5$	0.030	0.0514	14 655	0.045
$1.5 < i - W1 \leq 1.75$	0.032	0.0574	16 977	0.048
$1.75 < i - W1 \leq 2.0$	0.031	0.0553	16 885	0.047
$2.0 < i - W1 \leq 2.25$	0.028	0.0500	15 867	0.047
$2.25 < i - W1 \leq 2.5$	0.023	0.0479	14 690	0.055
$2.5 < i - W1 \leq 2.75$	0.017	0.0422	12 813	0.063
$2.75 < i - W1 \leq 3.0$	0.012	0.0362	10 959	0.076
$3.0 < i - W1 \leq 3.5$	0.013	0.0482	14 336	0.097
$3.5 < i - W1 \leq 4.0$	0.004	0.0183	5429	0.120
$i - W1 > 4.0$	0.002	0.0059	1846	0.100
i -band only	0.500	0.0409	11 841	0.002
$W1$ -band only	0.188	0.2146	65 658	0.030
Total	1.000	0.737	220 267	

Notes. The columns provide the details of the colour bin (magnitudes are in AB magnitudes), the fraction of the combined Pan-STARRS–WISE catalogue within that colour bin ($f_{\text{PS-WISE}}$), the iterated value of $Q_0(c)$, the final total number of LoTSS source matches to host galaxies of that colour (N_{LoTSS}) and the fraction of optical/IR sources in the combined Pan-STARRS–WISE catalogue of that colour that are a match to a LoTSS source down to the flux density limit of LoTSS (f_{radio}). We note that N_{LoTSS} include LR matches to sources included in LGZ associations as explained in Sect. 5.3, which amount to an average of 2% of the matches in each bin.

in $i - W1$ colour for those objects detected in both bands. These colour categories are detailed in Table 1. For each colour category, $n(m, c)$ was determined from the overall Pan-STARRS–WISE sample. The first-pass LR matches derived above were divided by colour and magnitude to provide the starting estimates of $q(m, c)$ and $Q_0(c)$.

These values were then used as the input to a LR analysis using both magnitude and colour, as per Eq. (3). Specifically, for this analysis, the i -band magnitude was used to determine the LRs within each colour bin, except for the “WISE-only” sources for which the $W1$ magnitude was used. As before, the (now colour-based) LRs were calculated for all sources in the combined Pan-STARRS–WISE catalogue within $15''$ of each radio source position.

From the resultant LRs of the most likely match to each radio source, the LR threshold corresponding to accepting a fraction $Q_0 = \sum_c Q_0(c)$ of identifications was adopted. The sources with $\text{LR} > L_{\text{thr}}$ then provided a modified set of matches, which was used to re-derive $q(m, c)$. The LRs of all of the Pan-STARRS–WISE sources were then re-evaluated using the new $q(m, c)$, which may lead to a change in the best-matching source or to a source moving above or below the LR threshold, and the process was iterated until an additional cycle provided no change in the adopted matches. This required five iterations, although the number of changes beyond the second iteration was largely negligible. We note that in order to avoid any risk of systematic bias against the rarest colour categories, a minimum value of 0.001 was set for each $Q_0(c)$; the iterative procedure could potentially cause $Q_0(c)$ to trend progressively towards zero. The final determined values of $Q_0(c)$ are provided in Table 1; summing these indicates that the total LR identification rate for LoTSS sources

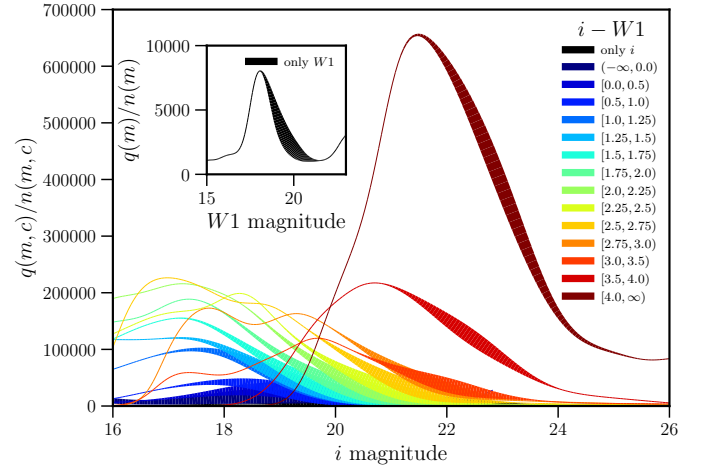


Fig. 1. Plots of $q(m, c)/n(m, c)$ for each colour bin of the LR analysis. Lines are colour-coded by galaxy colour bin (running naturally from blue to red); the width of the line is proportional to the number of LoTSS matches at that magnitude, i.e. thicker regions represent the most important regions for $q(m, c)/n(m, c)$ to be determined. The figure clearly demonstrates that the KDE approach for calculating $q(m, c)$ and $n(m, c)$ is able to produce broadly smooth versions of these functions with sufficient magnitude resolution. At fainter magnitudes, the ratio $q(m, c)/n(m, c)$ can be seen to rise monotonically and strongly towards redder colour bins, i.e. redder galaxies have a higher probability to host a radio source, as expected, except at the very brightest magnitudes where nearby star-forming (blue) galaxies contribute significantly.

is 73.7%. The derived $q(m)/n(m)$ functions in each colour bin are displayed in Fig. 1.

Final LRs were calculated using the iterated $q(m, c)$. A plot of the completeness and reliability of the final sample, as a function of LR threshold, is shown in Fig. 2. A threshold value of $L_{\text{thr}} = 0.639$ that corresponds to the point where the completeness and reliability cross was adopted (see Sect. 4.1.5). Both the completeness and the reliability are $\approx 99\%$.

Table 1 shows the number of accepted matches to LoTSS sources as a function of colour bin. It also shows the fraction of all galaxies within that colour bin that have a LoTSS counterpart, down to the flux density limit of LoTSS. This is also shown graphically in Fig. 3, and offers further motivation for the use of the colour-based LR analysis, since the probability of the reddest galaxies to host a radio source is an order of magnitude higher than those of the bluest galaxies.

Now that this has been determined for each colour bin, it can be applied to any further sample with properties similar to LoTSS. In particular, it can be used for LR analysis of new survey areas covered by LoTSS without need for new iterative calculation. We have also used this calibrated $q(m, c)$ to derive LRs for counterparts around the positions of the individual Gaussian components of multi-component PyBDSF sources, i.e. for each Gaussian component in the PyBDSF Gaussian catalogue, using the PyBDSF Gaussian catalogue as the basis catalogue (see also Sect. 6.6).

5. Visual identification and association with LGZ

Some sources are too large or complex to be reliably identified through the statistical LR technique described in the previous section. Moreover, the LR method cannot identify and correct cases where the source finder has not correctly grouped components of a single physical source together or where it

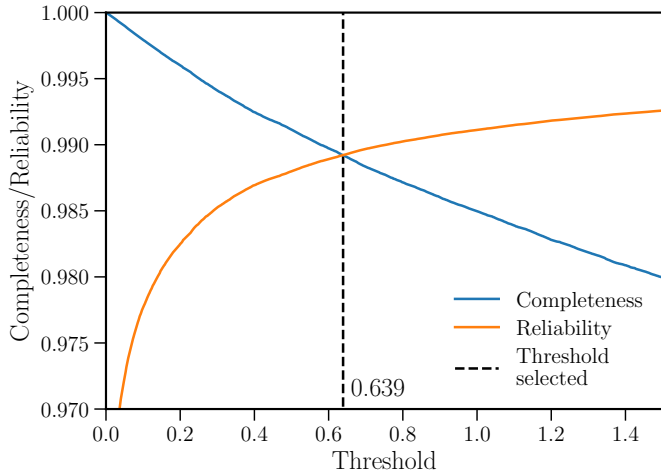


Fig. 2. Completeness and reliability of the host galaxy identifications as a function of the LR threshold. A threshold value of $L_{\text{thr}} = 0.639$ was adopted, corresponding to the point where the completeness and reliability cross.

has incorrectly grouped (blended) multiple physical sources together. Such association or deblending needs to be done separately; we do this and the optical/IR identification of large and complex sources through visual inspection. Based on the properties of the radio sources, we selected a subsample of sources to be handled this way; the details of the decision process are given in Sect. 6. In total, we selected around 13 000 PyBDSF sources that plausibly require visual inspection for optical/IR identification or source association.

In pilot projects we carried out this sort of process using manual tools that involved visual inspection of data stored on a local server by one or a few individuals (Williams et al. 2016; Hardcastle et al. 2016); but this is impractical for the HETDEX field and still more so for the larger sky areas that will be provided by the full LoTSS survey. Instead we used the Zooniverse⁸ framework and in particular the PANOPTES project builder⁹ to create an association and identification tool which we call LGZ and which is described in this section. At this stage of the LoTSS survey, access to LGZ through the web interface was limited to members of the LOFAR Surveys Key Science Project (KSP) and some of their close associates. Therefore although we use the standard Zooniverse terminology and describe the participants in the project as “volunteers” in what follows, it should be borne in mind that this is not citizen science and our volunteers all have some background in professional astronomy. The LGZ project should not be confused with the very similar Radio Galaxy Zoo project (Banfield et al. 2015), from which it draws some inspiration and which is a true citizen science project. Radio Galaxy Zoo itself is modelled on the original “Galaxy Zoo” (Lintott et al. 2008) project, which very successfully used citizen scientists to classify the morphologies of millions of galaxies in SDSS.

5.1. The LGZ interface

As in our pilot projects, we made the design decision to carry out in parallel the two processes of “association” (where the volunteer decides whether several sources in the PyBDSF catalogue should be treated as a single source) and “identification” (where

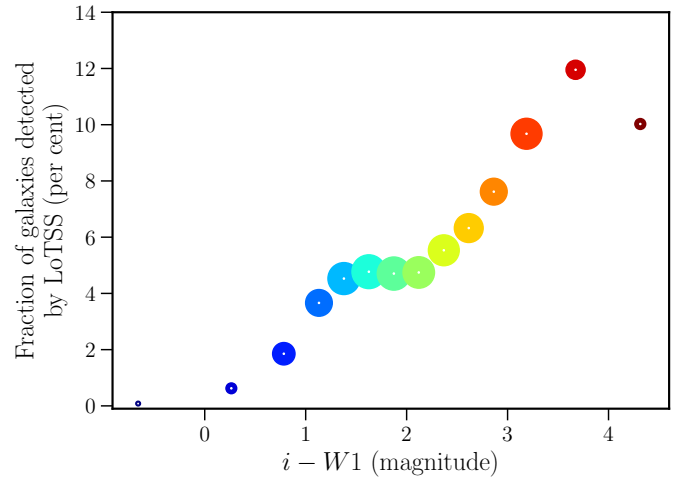


Fig. 3. Fraction of all galaxies within a particular colour bin that have a LoTSS counterpart down to the flux density limit of LoTSS. The colour of the symbols corresponds with the colour used in Fig. 1. The position along the x-axis is given by the average colour of all the sources in each bin. Poisson error is negligible and the error is dominated by misclassification and incompleteness. The size of the marker is proportional to the number of LoTSS sources matched. This plot demonstrates the additional power of using colour in the LR analysis owing to the much higher probability for red ($i - W1 > 3$) galaxies to host a radio source than for blue ($i - W1 < 2$) galaxies to do so.

the volunteer selects zero, one or more optical host galaxies for the possibly associated radio source). In many cases the position of a plausible optical host is very helpful in deciding on the correct source association, or vice versa. We therefore needed to present the volunteer with images to classify that showed the radio data and at least one optical image. After some experimentation, we chose to use both the Pan-STARRS r -band image and WISE band 1, together with radio contours from both the LoTSS images and the FIRST survey. The FIRST contours are used alongside LoTSS because flat-spectrum cores (which will appear strong in both LoTSS and FIRST), if present, are useful in pinpointing a host galaxy, though of course the majority of our sources have no FIRST counterpart. Pan-STARRS r -band is used for its good angular resolution; the ID fraction is only slightly lower than that of the i -band and the bluer wavelength provides a longer colour baseline. We use WISE band 1 because it is the most sensitive optical/IR band available to us for the typical elliptical hosts of radio-loud AGN (see Sect. 4), although its resolution is much lower than that of Pan-STARRS; at 6.1'' WISE band 1 is very comparable to the resolution of the LoTSS images themselves.

In order to present the images to volunteers in the PANOPTES framework we have to render them as static images for each PyBDSF source. After trials we settled on three images: one showing LoTSS and FIRST contours overlaid on a colour scale of the Pan-STARRS r -band image; one with only the r -band image, but with catalogued Pan-STARRS and WISE sources marked with (distinct) crosses; and one with the same contours as the first image, but overlaid on a colour scale of the WISE band-1 images. All images show ellipses which mark the location and size of the PyBDSF sources. The PANOPTES framework allows the volunteer to flip between these images at any time, either manually or with automatic cycling, so it is relatively easy to search for, for example the WISE counterpart of a Pan-STARRS source that might be a counterpart to a LoTSS target. Images were made using the APLPY PYTHON package

⁸ www.zooniverse.org

⁹ <https://github.com/zooniverse/Panoptes>

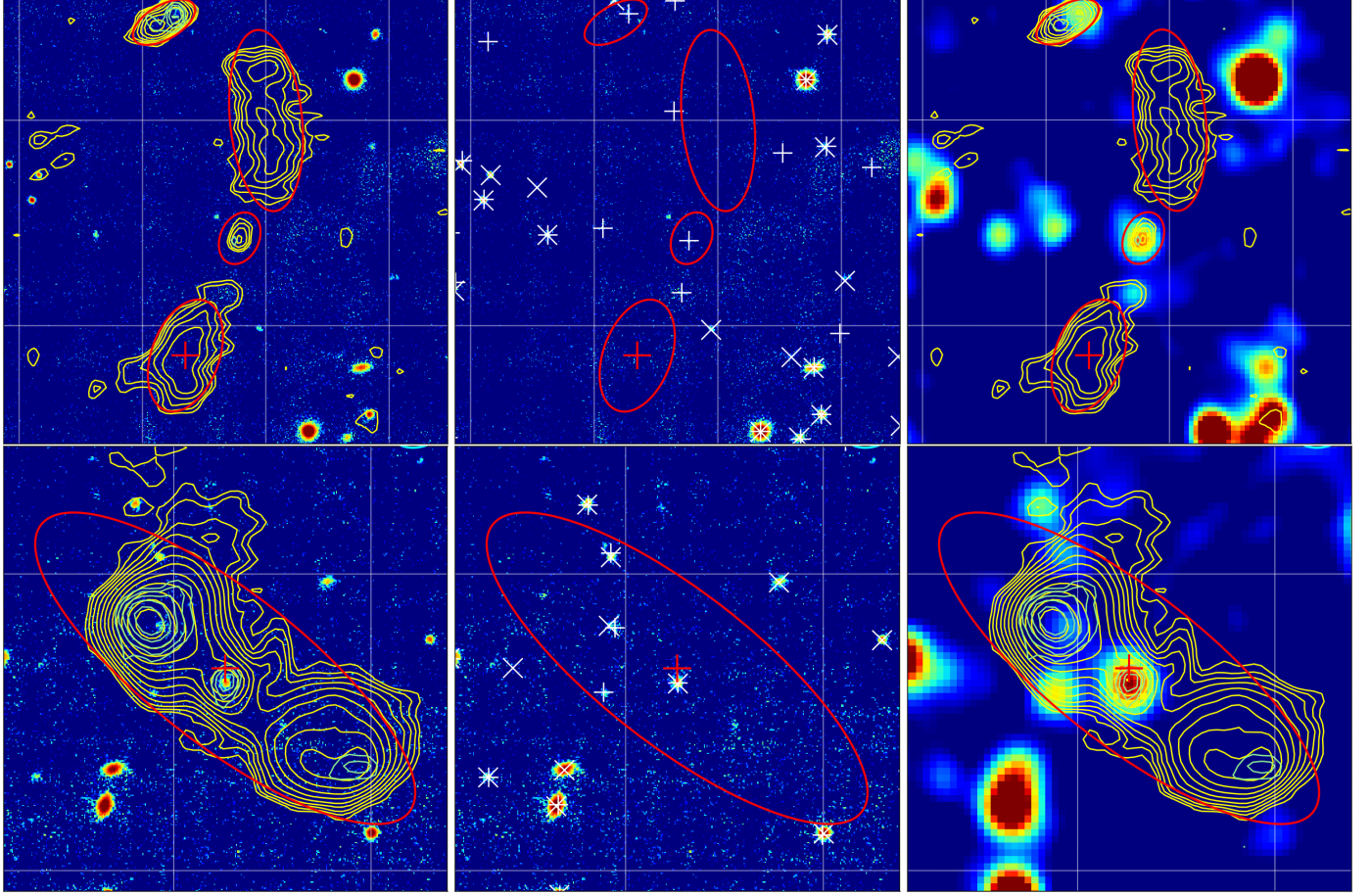


Fig. 4. Example set of images from LGZ for two different sources (*top* and *bottom panels*). *From left to right panels:* LoTSS (yellow contours), FIRST (green contours), and Pan-STARRS (colour); Pan-STARRS (colour) and Pan-STARRS and WISE catalogued sources (x 's and crosses, respectively); LoTSS, FIRST, and WISE band 1 (colour). The gridding interval in the vertical (N–S) direction is 1 arcmin. In the *top panels* the PyBDSF object of interest (indicated with the red cross) is a lobe of a radio galaxy. The volunteer should associate it with the core and northern lobe, but not with the smaller source on the northern edge of the image, which appears unrelated. No Pan-STARRS counterpart to the radio source is apparent, but there is a clear WISE band 1 detection and a marginal FIRST detection (green contours) co-located with the central LoTSS component, suggesting that this is very probably the host galaxy. In the *bottom panels* there is no other PyBDSF source to associate with the one of interest and there are clear Pan-STARRS and WISE detections coincident with the FIRST core.

(Robitaille & Bressert 2012); the colour and contour levels were determined based on the local image properties (e.g. local rms noise) and the peak flux density of the LoTSS source. Specifically, contours were drawn at a lowest level of twice the local rms noise level or 1/500 of the peak flux density of the component of interest, whichever was the higher, and increased by a factor of 2 from that lowest level. The size of the region to be displayed was based on both the size of the PyBDSF source of interest and on the locations of potential association candidates, using an iterative NN algorithm with some constraints to prevent the field of view of the image becoming too large or excluding the original source. Two example image sets are shown in Fig. 4.

The volunteer can access all three of these images while responding to the following three sets of instructions:

1. Select additional source components that go with the LoTSS source marked with the cross. If none, do not select anything.
2. Select all the plausible optical/IR identifications. If there is no plausible candidate host galaxy, do not select anything.
3. Answer the questions: Is this an artefact? Is more than one source blended in the current ellipse? Is the image too zoomed in to see all the components? Is one of the images missing? Is the optical host galaxy broken into many optical components?

Answers to these must be provided in order. For tasks (1) and (2) the user clicks on the image and the location of their click is stored. For task (3) the user checks one or more boxes if the answer to the corresponding question is “yes”. The purpose of task (3) is to ensure that common problems with the classification are flagged by the user. Once all questions are answered, the user can move to the next PyBDSF source.

The Zooniverse interface presents all images to all volunteers until a given image has been seen a predetermined number of times, after which it is “retired” and will no longer be presented to volunteers. Originally, we set the retirement limit to ten – that is, each image must be classified by ten volunteers before it is retired – but after some experimentation we found that we were able to reduce the limit to five in the course of the classification process while still recovering good classifications. A feature of the fact that we present PyBDSF sources to the volunteers is that a complex physical source containing a large number of PyBDSF source components will be seen more times than a simple one. For example, the top source shown in Fig. 4 will have been seen at least ten times because both the northern and southern lobe of the radio galaxy meet the selection criterion for visual inspection. We note that the PyBDSF source marking the core of the radio galaxy in this example would not have been

included in the LGZ sample because of its compact nature but is included in the output LGZ association. The bottom source in Fig. 4 will only be seen five times.

The LGZ project was carried out in two phases, the first (LGZ v1) was the inspection of about 7000 bright, extended sources in the early part of the decision tree (branch A), and the second (LGZ v2) involved around 9000 later decision tree end-points. In LGZ v2 associations from the decision tree and from LGZ v1 were highlighted with different colours of ellipses and some improvements were made to the code to determine field of view, but otherwise there were no significant differences between the two parts of the project. One point to note is that LGZ v1 was started with an earlier round of processing of the LoTSS images and as a result there were some differences between the input PyBDSF catalogue for LGZ v1 and the final catalogue by the time LGZ was complete. These differences were resolved by cross-matching of the two catalogues in post-processing and have little effect on the final results.

5.2. LGZ output

As with all PANOPTES results, LGZ outputs are provided in a JSON file which gives details of the location (in pixel terms) of each mouse-click on an image and of the answers to the questions asked under task (3) above. These raw results were converted to selections of PyBDSF sources and optical sources using the underlying catalogues. For the source association, task (1), clicks were matched to PyBDSF sources by identifying all sources enclosing the click position, and then in the case of multiple (overlapping) sources at the click position, selecting the source whose centre is closest to the click position. For the optical/IR identifications, task (2), click positions were matched to catalogued galaxies by selecting the nearest galaxy in the combined PanSTARRS-WISE catalogue to the click position, provided the separation distance was less than $1.5''$. The latter criterion was applied to exclude a minority of spurious/accidental clicks; this threshold was optimised using visual inspection. We then looked for consensus in both the association and identification.

For each input LGZ source, we considered all sets of PyBDSF sources associated together by at least one viewer (where a “set” contains one or more PyBDSF sources), assigning the association set quality (LGZ_Assoc_Qual) to be the fraction of all views of this source region for which the listed association was chosen as the associated set. Those associated sets with $\text{LGZ_Assoc_Qual} > 2/3$ were then considered as candidate sources for the final catalogue. Because some sets may be subsets of others, there may be more than one set for a given source that meets this threshold; for each input source we selected for the final catalogue the largest set that included that source and met the quality threshold. In a small number of cases, resulting from non-optimal image sizes not flagged as problematic via the LGZ process, peripheral source components (e.g. small/faint components that were not in the LGZ input sample) ended up in multiple sets. Such overlaps, which were trivially detected in the final catalogue by checking for PyBDSF sources that lay in more than one set, were resolved by visual inspection.

Once the associated sources were finalised, the LGZ optical IDs were determined in a similar way: all optical/IR identifications made by at least one viewer were assigned an ID quality (LGZ_ID_Qual) corresponding to the fraction of source views in which this ID was selected as the correct one. If there was a single ID selected in more than two-thirds of source views, this was retained for the final catalogue. For both the final association of PyBDSF sources and optical IDs, the quality flags

(corresponding to the fraction of views for which the catalogued outcome was selected) were retained in the final catalogue, allowing for more stringent cuts to be made in later analysis.

Sources that emerge from LGZ with flags set to indicate that there were a significant number of positive answers in task (3) are dealt with in special ways. Where a majority (more than 50%) of volunteers agree in classifying a source as an artefact, that source is removed entirely from the final catalogue. Several hundred dynamic-range artefacts around bright sources (see Sect. 6.1) were removed in this way. If a significant fraction of volunteers (more than 40%) classed a source as “too zoomed in” – i.e. the field of view presented to them was in their opinion not large enough to carry out the association or identification correctly – then that source was re-inspected by a single expert using a PYTHON-based interactive tool that generates similar images but with the ability to pan and zoom, using the volunteers’ association as a starting point, and new sources (and potentially a revised optical ID, to be processed in the same way as other LGZ optical IDs) were added to the association if necessary. Sources flagged as blends by more than 40% of viewers were examined in the deblending workflow (see Sect. 5.4). Sources where the host galaxy was flagged as broken up in the optical catalogue by more than 50% of viewers were simply associated with the nearest bright optical galaxy from the 2MASX catalogue, as these were confirmed to be exclusively associated with optical sources so bright that the PanSTARRS or WISE cataloguing algorithms had failed. In this case we record the name of the 2MASX match, but take the position from the nearest match for that 2MASX source in the merged Pan-STARRS/AllWISE catalogue. The flag to indicate that an image was missing was hardly used; we inspected visually all four sources where more than 50% of viewers selected this option and verified that they were treated appropriately by the default processing.

5.3. Associated sources

In the following, associated sources refer to those where separate PyBDSF sources have been associated and combined into single new physical sources either based on the LGZ output or matches with large optical galaxies (see Sect. 6.2). The individual PyBDSF sources that make up (i.e. are components of) associated sources were removed from the final LoTSS-DR1 value-added catalogue and replaced with the associated sources, such that the final catalogue should, to the best of our ability, contain only true physical radio sources. We note that LGZ associations can include PyBDSF sources from other outcomes of the decision tree described in Sect. 6, in which case the LGZ association takes precedence.

For all associated sources, we generated the LoTSS source properties and populated the relevant table columns (total flux density, size, radio position, and radio source name) by combining the properties of their constituent PyBDSF sources (or PyBDSF Gaussian components in the case of blends – see next section). Some of these combinations are obvious but it is worth commenting on a few of them. The position of the source was taken to be the flux-weighted mean of the positions of each component. For the total flux density, we simply summed the total flux densities of each component. Previous work has shown that this normally gives a reasonably accurate flux density measurement compared to hand-drawn integration regions, as long as PyBDSF has captured all the flux density; this is likely to go wrong in for example very large diffuse regions where PyBDSF fails to distinguish source from background. For each of these properties we propagated the errors of the component

parameters as appropriate. The peak flux density of the associated source was taken to be the maximum value of the peak flux densities of the component sources, along with its corresponding error. The rms was taken to be the mean value of the rms for the component sources. The *S_Code* was updated based on the number of Gaussian components in the new source; “S” for a single Gaussian component and “M” for multiple.

To determine source sizes we used the convex hull around the set of elliptical Gaussians: the convex hull is the smallest convex shape that contains all of the ellipses. To construct the convex hull we represented each component (PyBDSF source or PyBDSF Gaussian as appropriate) as an ellipse, where the deconvolved FWHM major and minor axes are taken to be, respectively, the semi-major and semi-minor axes of the ellipse. The convex hull was constructed around all of the component ellipses using the *SHAPELY PYTHON* package. Then we took the size of the source (“*LGZ_Size*”) to be the length of the largest diameter of the convex hull around the set of elliptical Gaussians; that is, for all points on the convex hull considered pairwise, we found the maximum vector separation, and took its magnitude. The source position angle (“*LGZ_PA*”) was taken to be the position angle on the sky of that largest diameter vector. For the source width (“*LGZ_Width*”) we adopted twice the maximum perpendicular distance of points on the convex hull to the largest diameter vector. These definitions have the feature that, if applied to a single ellipse, they return the major and minor axis of the Gaussian and its position angle. Source sizes determined from the maximum distance between components, as in [Hardcastle et al. \(2016\)](#), can be significant underestimates where the components are extended: the present approach is likely to overestimate the true size in general but gives results in better agreement with measurements by hand. We do not provide error estimates for the shape parameters in the final catalogue.

5.4. Deblending workflow

Blended sources, either from LGZ or from the “M” source decision tree (see Sect. 6.6), were examined in a specific deblending workflow involving a *PYTHON*-based interactive visual inspection by a single expert. Each PyBDSF source was first split into its Gaussian components as originally fitted by PyBDSF. These Gaussians were then re-associated as appropriate into new radio sources and identified with zero or more optical counterparts, which were handled in exactly the same way as optical counterparts found by LGZ. Around 1500 sources were dealt with in this way.

In the final LoTSS-DR1 value-added catalogue, PyBDSF sources that were identified as blends and processed in the deblending workflow were removed and replaced by sources made by combining their component Gaussians; they therefore have properties (flux densities, sizes, etc.) appropriate for associated sources. The properties of the Gaussian components are combined into single sources in the same way that the component PyBDSF sources are combined for associated sources as described in Sect. 5.3, except that we use the parameters (total flux density, position, etc.) from the PyBDSF Gaussian catalogue. Notably, for the positions and sizes, this is not exactly the same process by which PyBDSF combines the fitted Gaussians into sources, which is based on image moment analysis, but produces comparatively similar results.

6. Decision tree

In this section we describe how we select which radio sources to process using the statistical LR and visual LGZ methods. We

also discuss any sources that need to be handled differently. In order to reduce the number of sources that were passed to some form of visual inspection, all 325 694 sources in the PyBDSF catalogue were evaluated through a decision tree to select sub-samples of sources that required (i) direct visual association and identification via LGZ; (ii) visual sorting into one of several categories, including selection for LGZ; (iii) rejection as artefact; or (iv) identification through LR analysis. We describe the main decisions taken, with approximate numbers/fractions of sources at each stage. A graphic representation is shown in Fig. 5, and key parameters are defined in Table 2 and described in detail in this section. A separate process is followed within the decision tree for PyBDSF sources fitted with multiple Gaussians. This process is illustrated in Fig. 6, and key parameters are defined in Table 3 and described in detail in Sect. 6.6. These figures and tables are best read as a high-level summary in conjunction with the detailed descriptions in the text.

Some stages of the decision tree required “visual sorting” (pre-filtering) prior to including sources in the LGZ sample, i.e. to avoid overpopulating the LGZ sample with unnecessary sources we filtered them beforehand. For this visual sorting, images similar to those used for LGZ (Pan-STARRS *r*-band images with radio contours from both the LoTSS images and the FIRST survey) were produced and rapidly inspected to categorise the sources relevant to that stage of the decision tree. This was done by a small number of experienced people, using a simple *PYTHON* interface to view and categorise the images where each source was viewed by one person only¹⁰. The aim of these steps was only to quickly pre-filter the list such that the LGZ sample remained manageable and included only the necessary sources; i.e. the LGZ sample was not polluted by vast numbers of sources which were either clear artefacts or clearly suitable for automated statistical analysis. The aim was not to also make the LGZ classification as this would slow down the process and because visual classifications in LGZ are made by consensus by several people.

6.1. Artefacts

Owing to the dynamic range limitations in the imaging (see Sect. 3.4 in [DR1-III](#)), the PyBDSF catalogue contains a not insignificant number of spurious sources or artefacts. These are generally found near the brightest compact sources in the images. Typically these consist of either several small artefacts detected in the vicinity of the bright source, or large artefacts in the vicinity of the bright source picked up at the higher order wavelet scales of the source detection. Since these are not real sources, they need to be flagged as such and removed from the final catalogue.

An initial selection of candidate artefacts was made by considering all compact bright sources (brighter than 5 mJy and smaller than 15”) and selecting their neighbours within 10” that are 1.5 times larger. This selects large sources in close proximity to compact, bright sources. Since such structures can in fact be real, for example faint lobes near a bright radio core, these candidate artefacts were visually confirmed. Out of 884 (83%) of such candidate sources 733 were confirmed as artefacts. We note that, as a preliminary step, this was not a complete artefact selection; for example it did not select clusters of artefacts around bright sources. Further work can be done to improve the identification of artefacts at this early stage in the decision tree, although future improvements in LOFAR imaging will also reduce the

¹⁰ In practice source lists were split between several people, each of whom could categorise tens of sources per minute.

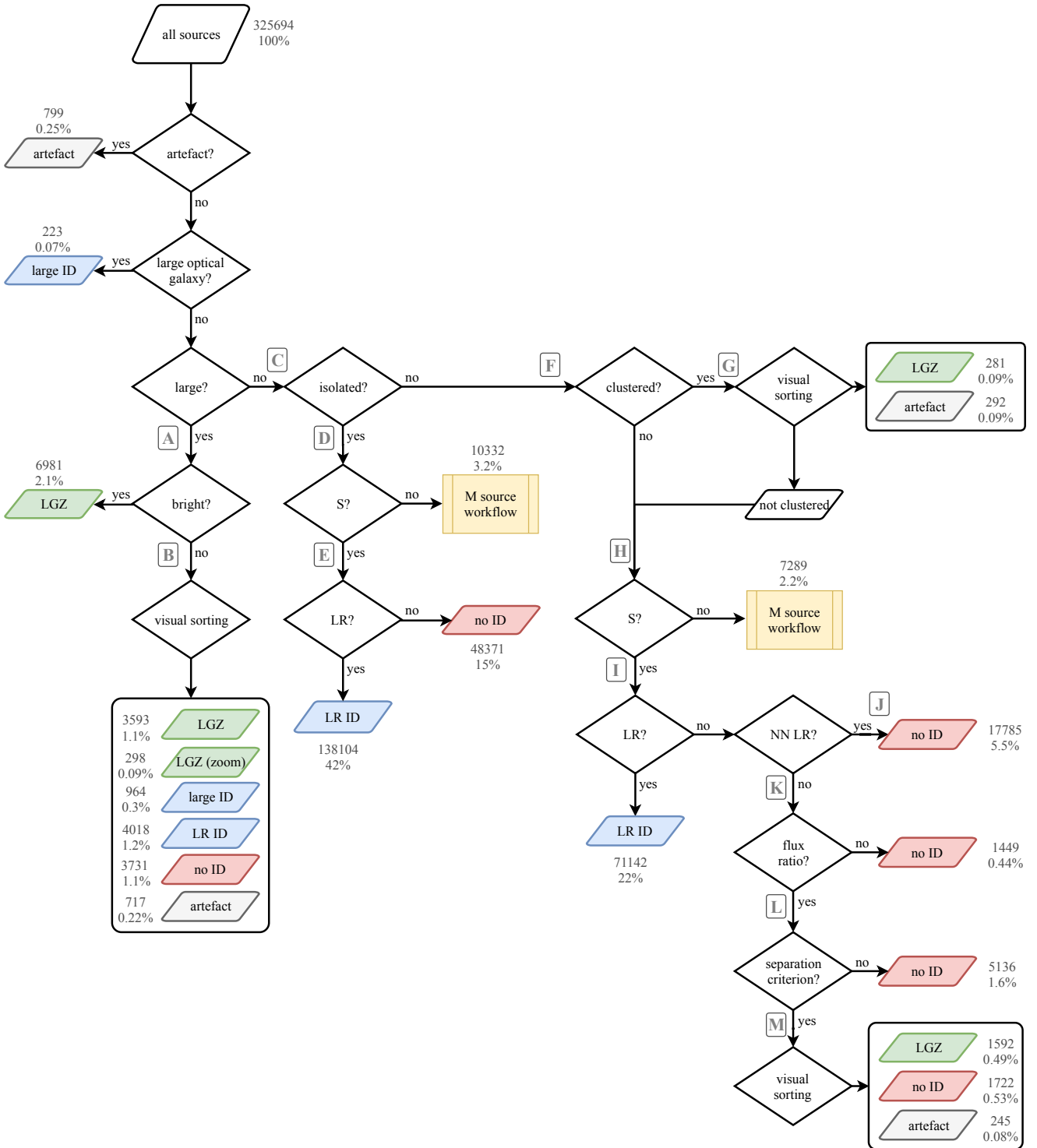


Fig. 5. High level summary of the decision tree used to process all entries in the PyBDSF catalogue. Following this workflow a decision is made for each source whether to: (i) make the optical/IR identification, or lack thereof, through the LR method (blue and red outcomes respectively); (ii) process the source in LGZ (green outcomes); (iii) reject the source as an artefact (grey outcomes); or (iv) process further in a separate workflow (yellow outcomes: see Fig. 6). The key parameters are defined in Table 2 and full details of the decisions are given in Sect. 6, with reference to the branch labels A–M. The numbers reflect the number of PyBDSF sources in each final bin and the percentage is relative to the total number of sources in the PyBDSF catalogue.

number of artefacts. Artefacts were also identified in all further stages of visual sorting within the decision tree described here. Finally, the LGZ output included an artefact classification (see Sect. 5.2).

Images from pointings on the outer edges of the DR1 coverage have hard edges and a small number of sources can be cut

off. Sources may still be detected by PyBDSF at the edges of an image, but such sources are likely to be incomplete or have erroneous flux densities and shapes. We have therefore flagged and removed ~200 sources where the fitted PyBDSF shape overlapped the edge of the mosaic, or where the source overlapped another edge source.

Table 2. Definition of the parameters used in the main decision tree in Fig. 5.

Parameter	Definition
Large optical galaxy	2MASX size ($r_{\text{ext}} \geq 60''$)
Large	PyBDSF major axis $> 15''$
Bright	Total flux density > 10 mJy
Isolated	Distance to nearest PyBDSF neighbour (NN) $> 45''$
S	Single Gaussian component within an island
LR	LR > 0.639
Clustered	Distance to fourth nearest PyBDSF neighbour $< 45''$
NN LR	LR _{NN} > 0.639
Flux ratio	$S/S_{\text{NN}} < 10$
Separation criterion	$S + S_{\text{NN}} \leq 50(d_{\text{NN}}/100'')^2$ mJy

Notes. See Sect. 6 for details.

A total of 2543 sources ($\sim 1\%$) were flagged in the PyBDSF catalogue (and an artefact flag column was added to the catalogue presented in DR1-I) through the artefact selection and various visual sorting and LGZ stages. These sources were dropped from further analysis and are not included in the final catalogues presented here.

6.2. Large optical galaxies

The radio emission associated with nearby galaxies that are extended on arcminute scales in the optical is clearly resolved in the LoTSS maps and can be incorrectly decomposed into as many as several tens of sources in the PyBDSF catalogue. To deal with these sources we selected all sources in the 2MASX catalogue larger than $60''$ and for each, searched for all the PyBDSF sources that are located (within their errors) within the ellipse defined by the 2MASX source parameters (using the semi-major axis, “ r_{ext} ”, the K_s -band axis ratio, “ k_{ba} ”, and K_s -band position angle, “ k_{pa} ”). The PyBDSF sources were then automatically associated as a single physical source and identified with the 2MASX source. We record the 2MASX source name as the the ID_name of the LoTSS source, but take the co-ordinates and optical/IR photometry from the nearest match in the combined Pan-STARRS–AllWISE catalogue, with the caveat that the PanSTARRS and AllWISE photometry is likely to be wrong for these large sources. This reduced the demands on visual inspection at the LGZ stage and avoided the possibility of human volunteers missing out components of the radio emission from the galaxy in their classification.

6.3. Large radio sources

Since the size of a source is a first indication whether it is resolved and possibly complex, we first considered the sources that are large ($>15''$, branch A in Fig. 5). This constitutes around 6% of the sample. All large, bright sources (brighter than 10 mJy) were selected for visual processing in LGZ¹¹. Containing around 7000 sources, this constitutes around 2% of the PyBDSF catalogue.

Instead of also directly processing the remaining ~ 13 k large, faint sources (fainter than 10 mJy – branch B) in LGZ, these sources were first visually sorted as (i) an artefact; (ii) com-

plex structure to be processed in LGZ; (iii) complex structure, where the emission is clearly on very large scales, to be processed directly in the LGZ “too zoomed in” post-processing step (see Sect. 5.2); (iv) having no possible match; (v) having an acceptable LR match, i.e. LR ID; or (vi) associated with an optically bright/large galaxy. It should be noted that within this category of large, faint radio sources, those larger than $30''$ are too large to have a LR estimate and so we included option (vi) to allow an identification with the nearest large/bright optical galaxy based on the Pan-STARRS images. The ~ 1000 such sources with a visually confirmed large optical galaxy match were then matched directly to the nearest 2MASX source, or in the 35 cases where there was no 2MASX source, to the nearest bright SDSS source. In all cases the nearest 2MASX or SDSS match was confirmed to be the correct match. Again the ID positions for these sources are taken from the nearest matches in the merged Pan-STARRS/AllWISE catalogue. An additional ~ 4000 sources were included in the LGZ sample after this visual sorting on branch B.

6.4. Compact radio sources

Sources $<15''$ in size make up around 94% of the PyBDSF catalogue (branch C). While many of these are individual sources best processed using the LR method, a subset are components of complex sources. Visual inspection of the entire catalogue was impossible given the available effort, so we applied a series of tests to select those small sources most likely to be components of complex sources. We initially considered whether the sources smaller than $15''$ have any nearby neighbours. Sources where the distance to the NN is greater than $45''$ were considered to be isolated (branch D; ≈ 200 k sources). A separation of $45''$ corresponds to a linear distance of 230–330 kpc at redshifts of 0.35–0.7, where the bulk of the AGN population of this sample is located (see DR1-III)¹². Before directly accepting the LR results for these sources, we removed those that were fitted by PyBDSF using multiple Gaussian components or those that lay in islands with other sources (i.e. with catalogued “S_Code” values of “M” or “C”); in these cases (≈ 10 k sources) a further decision tree was followed, taking into account the LR matches to the individual Gaussian components of the source (see Sect. 6.6). For the

¹¹ For the first phase of LGZ processing (see Sect. 5), all large, bright sources in the PyBDSF catalogue were selected and so the LGZ v1 sample included some of the artefacts and components of large optical galaxies discussed in Sects. 6.1 and 6.2

¹² In the LOFAR samples of Hardcastle et al. (2016) and Williams et al. (2016), in which the association and identification was done entirely visually, 66% of the sources (i.e. including separate components of AGN) are smaller than $45''$. However this does not mean that we miss larger sources as these are picked up in other parts of the decision tree.

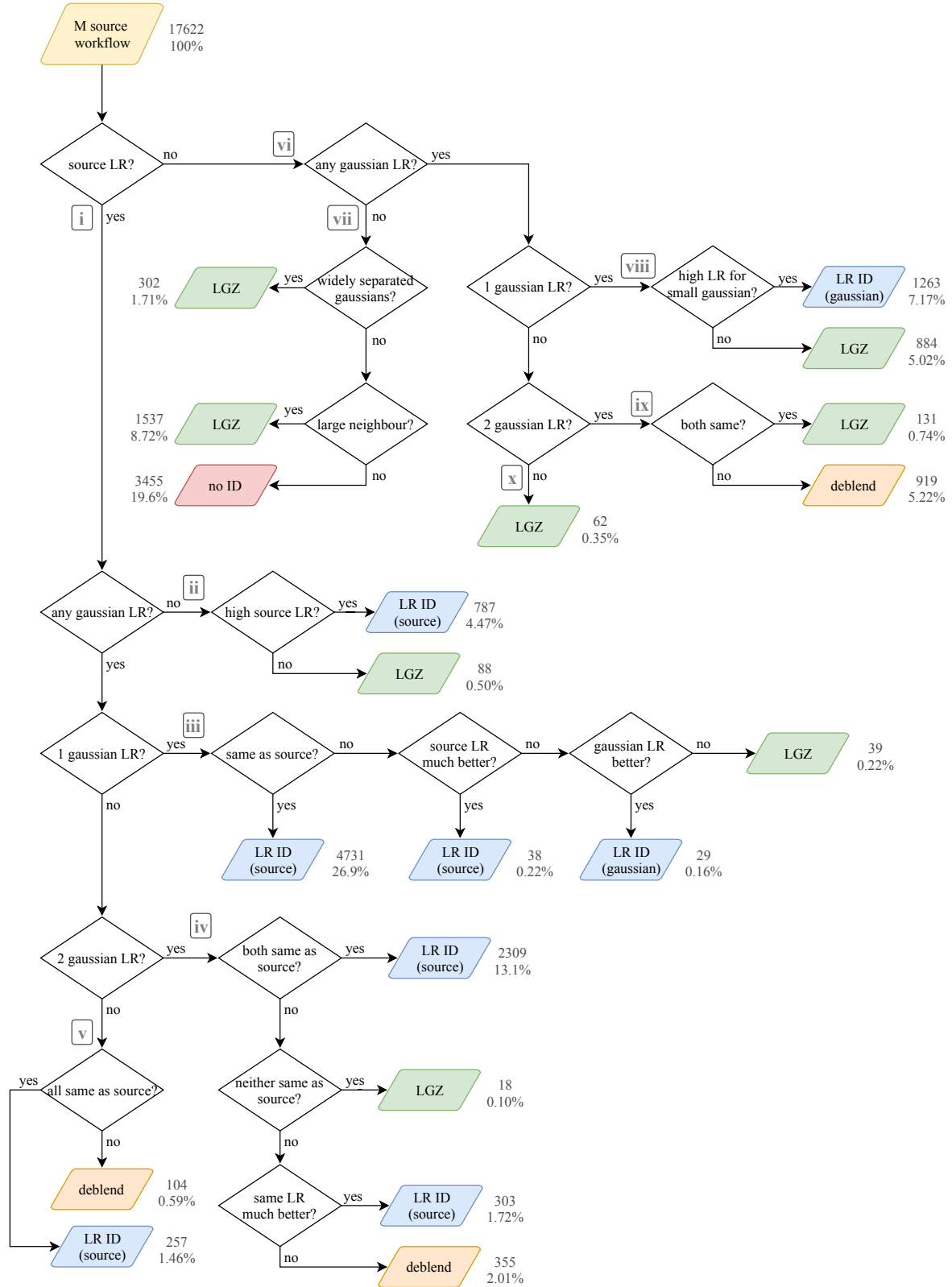


Fig. 6. High level summary of the decision tree used to process all compact “M” sources (i.e. PyBDSF sources fitted with multiple Gaussians) in the PyBDSF catalogue. Following this workflow a decision is made for each source whether to: (i) make the optical/IR identification, or lack thereof, through the LR method (blue and red outcomes respectively) for either the PyBDSF source or one of the Gaussian components; (ii) process the source in LGZ (green outcomes); or (iii) process further in a separate deblending workflow (orange outcomes, see Sect. 5.4). The key parameters are defined in Table 3 and full details of the decisions are given in Sect 6.6, with reference to the branch labels i–x. The numbers reflect the number of PyBDSF sources in each final bin and the percentage is relative to the total number of compact “M” sources in the PyBDSF catalogue.

Table 3. Definition of the parameters used in the decision tree for “M” sources (i.e. PyBDSF sources fitted with multiple Gaussians) in Fig. 6.

Parameter	Definition
Source LR	$LR_{\text{source}} > 0.639$
Any Gaussian LR	At least one Gaussian component has $LR_{\text{gauss}} > 0.639$
High source LR	$LR_{\text{source}} > 6.39$
N Gaussian LR	N Gaussian components have $LR_{\text{gauss}} > 0.639$
Same as source	The ID(s) for the Gaussian component(s) are identical to the ID for the source
Source LR much better	$LR_{\text{source}} > 10 \ \& \ LR_{\text{gauss}} < 10 \ \& \ LR_{\text{source}} > 10LR_{\text{gauss}}$
Gaussian LR better	$LR_{\text{gauss}} > 10 \ \& \ LR_{\text{source}} < 10 \ \& \ LR_{\text{gauss}} > 10LR_{\text{source}}$
Same LR much better	$LR_{\text{source}} > 100 \ \& \ LR_{\text{gauss(same)}} > 5LR_{\text{gauss(different)}}$
Widely separated Gaussians	Maximum separation between Gaussian components of the PyBDSF source larger than $15''$
Large neighbour	Large ($>10''$) neighbour within $100''$
High LR for small Gaussians	$LR_{\text{gauss}} > 6.39$ & the Gaussian size is $< 10''$

Notes. See Sect. 6.6 for details.

remaining small, isolated, single Gaussian-component sources (i.e. with catalogued “S_Code” values of “S”), we accepted the LR results (branch E): either the source has an acceptable LR match (LR ID) or it has no acceptable LR match (no ID).

Small sources that are not isolated (i.e. have at least one other source within $45''$ – branch F) have a higher chance of being a component of a complex source. For these sources we considered whether they are clustered to some extent, based on the distance to the fourth neighbouring source: for approximately 1100 sources this distance is less than $45''$ (branch G). Empirically, based on visually examining subsamples of sources, we found that taking the fourth NN maximised the number of genuinely clustered sources while minimising the number of unrelated sources. As these may be part of a larger structure or simply chance groups of unassociated sources that can be matched by the LR method, we visually sorted such clustered sources either as (i) complex (to be sent to LGZ), (ii) not complex (appropriate for further analysis in the decision tree), or (iii) as an artefact. About a quarter of the clustered (branch G) sources were selected for LGZ, while about another quarter were flagged as artefacts. The remainder were considered not clustered based on the visual sorting and assessed via branch H.

For the remaining small, non-isolated, but not clustered sources (branch H), those that have multiple Gaussian components were again treated in a separate workflow (see Sect. 6.6). We then considered whether the source and/or its NN have a LR match above the threshold (branch I). In the case where the source has an LR match, we accepted the LR identification. In the case where the source of interest has no LR match, but its NN does, we accepted that the source has no match (branch J). However, in the case where neither the source nor its NN has an acceptable LR match (branch K), it is increasingly likely that the two sources are part of a complex structure where the optical ID is not coincident with either radio component. For such pairs, we further considered the flux ratio of the source to its NN. Sources with extreme flux density ratios are less likely to be associated. We made a somewhat conservative cut at a flux density ratio of 10 (see e.g. Prandoni et al. 2000), and for sources with ratios larger than 10 we accepted that there is no LR match. We then applied a flux-dependent separation criterion for the sources with similar fluxes (branch L), following Huynh et al. (2005), of $S + S_{\text{NN}} \leq K(d_{\text{NN}}/100'')^2$, where S and S_{NN} are the total flux density of the source of interest and its NN, respectively, and d_{NN} is their separation in arcsec. The constant K ($= 10$ mJy in Huynh et al. 2005) was adjusted to take into account the different working frequency (150 MHz instead of 1.4 GHz). We adopted $K = 50$ mJy,

under the assumption of steep spectrum radio sources ($\alpha = -0.7$). For sources that did not meet this criterion we accepted that there is no LR match, while for those ~ 3500 that did (branch M) we did a final stage of visual sorting to (i) select as a possible group for LGZ association and identification, (ii) accept that there is no match, or (iii) classify as artefact. These sources were split roughly equally between the first two options and a further ~ 200 sources were flagged as artefacts.

6.5. Radio source pairs

The final steps (branches J–M) of the decision tree consider only the NN to a given source and not all possible neighbours. To ensure that we did not miss any double sources where another unassociated source lies nearer to one of the sources than the separation between the pair, we selected all the pairs of sources that meet the above flux ratio and flux-dependent separation criteria and that also consist of two sources with multiple Gaussian components. To try to capture more large radio galaxies, we considered all such pairs with separations of up to $60''$, not already included in the LGZ sample¹³. These ~ 3200 sources were visually sorted and ~ 1500 (46%) more potentially genuine double sources were included in the LGZ sample. Sources not included in LGZ keep their classification from the decision tree. This step is not shown on the decision tree because it includes sources from several different outcomes.

6.6. Sources with multiple Gaussian components – “M” sources

Within the decision tree the largest sources are all visually inspected, either directly in LGZ or through visual sorting; however, sources that are small ($< 15''$) may still be resolved and may have been fitted by multiple Gaussian components by PyBDSF. Such sources are identified in the PyBDSF catalogue with a value of “M” in the “S_Code” column, and we refer to these in what follows as “M” sources. In this category, we include also the 102 sources with “S_Code” values of “C”, i.e. sources fitted with a single Gaussian component, but which lie in the same island as other source(s). There are about 18k compact “M” sources, 10k of which are isolated. Such sources may be unambiguous single sources with substructure (e.g. the two

¹³ Although many giant radio galaxies will be picked up in LGZ, the final value-added catalogue may be incomplete for some truly giant radio galaxies, in particular those made up of two widely separated compact lobes.

lobes of a radio galaxy) or may be two or more nearby distinct sources that have been grouped as a single source by PyBDSF, i.e. blended sources. An additional complication is that calibration errors and dynamic range limitations lead to shape distortions, resulting in multiple Gaussian components being fitted by PyBDSF to a single source. Moreover, true extended radio sources are not necessarily Gaussian in shape or even composed of the sum of Gaussian shapes. This is a choice of representation imposed by our source detection algorithm. These factors, and intrinsic asymmetries in the sources (e.g. head-tail sources), mean that even in the case of single sources, the flux-weighted source positions provided by PyBDSF may not coincide with the optical host galaxy positions, making the LR values unreliable. Nevertheless, combining the information in the LR matches to both the overall source and to the individual Gaussian components provides a means to diagnose specific cases and either allow an LR result to be obtained for a source or to identify cases for further visual inspection and deblending.

These compact “M” sources may be isolated or not, but were treated in a separate “M source” workflow, in which we also considered any LR matches to the individual Gaussian components of each source. A schematic overview of this decision tree is given in Fig. 6, and key parameters are defined in Table 3 and described in detail in the following subsections. The only difference between isolated and non-isolated “M” sources is that non-isolated sources were subjected to additional visual sorting before inclusion in the LGZ sample; for clarity this is not shown explicitly in Fig. 6, but each decision that ends in “LGZ” for the non-isolated sources can be taken to mean “visually confirmed for LGZ” otherwise the alternate decision was followed, while for the isolated sources they were directly added to the LGZ sample. The final decisions were to accept the source LR match, accept one of the Gaussian LR matches, include the source in the LGZ sample (where one of the possible outcomes is blended; see Section 5), or pass the source directly to a separate deblending workflow (see Sect. 5.4).

6.6.1. Sources with a LR identification

We first considered whether the source has a LR match above the threshold (branch i in Fig. 6), then whether at least one of the Gaussian components has an LR match above the threshold, and subsequently tried to resolve any ambiguities in the optical matches to the source and Gaussian components. If none of the Gaussian components have a good LR match (branch ii), then the source match was accepted provided the LR exceeded a higher threshold; a threshold ten times normal ($LR > 10L_{\text{thr}} = 6.39$) was used because “M” sources often have larger uncertainties on their source positions, which can lead to lower LR misidentifications, especially for sources lying in over-dense environments. Otherwise the source was included in the LGZ sample for closer inspection. A high threshold source LR match with no good Gaussian LR matches generally occurs when a slightly resolved double radio source is composed of two (or more) Gaussian components which are correctly grouped by PyBDSF as a source whose position corresponds to the optical ID.

When only one Gaussian component has an LR identification (branch iii), the majority of the time it is the same optical/IR source as the source match and the identification is unambiguous. In the remaining few cases, where the single Gaussian component LR match is different to the source match, we evaluated whether one is significantly better than the other. The source match was accepted only if the source LR exceeds a higher threshold and exceeds ten times that of the Gaussian

component: $LR_{\text{source}} > 10 \ \& \ LR_{\text{gauss}} < 10 \ \& \ LR_{\text{source}} > 10LR_{\text{gauss}}$. Likewise, the Gaussian component LR match was preferred to that of the overall source under the reverse conditions: $LR_{\text{gauss}} > 10 \ \& \ LR_{\text{source}} < 10 \ \& \ LR_{\text{gauss}} > 10LR_{\text{source}}$. These ranges were chosen empirically based on visual inspection of images of subsamples of sources. The remaining in-between cases, where neither the source nor the Gaussian component LR match can be deemed to be reliably better by statistical methods only, were evaluated in LGZ.

The situation is more complex if more than one Gaussian component has an acceptable LR match. In roughly three-quarters of the cases in which two Gaussian components have LR matches (branch iv), both Gaussian components match the same optical source as the radio source LR match, so the identification could be unambiguously accepted. Another quarter fall into the category where one Gaussian component match is the same as the source match. Some of these were deemed to have a very good source match ($LR_{\text{source}} > 100 \ \& \ LR_{\text{gauss(same)}} > 5LR_{\text{gauss(different)}}$) and so the source match was accepted. The rest were processed in the deblending workflow. For a small number of sources, the two Gaussian component matches and source match are all different. These sources were processed in LGZ.

Finally, only a small number of sources have three or more Gaussian components with LR matches (branch v), and in this case about three quarters all unambiguously match the same optical source as the source LR match, which was then accepted, while the remainder were processed via the deblending workflow.

6.6.2. Sources without a LR identification

The second major branch of this decision tree considers the case where there is no good LR match to the overall source (branch vi). If these are isolated sources, then they may simply have no counterpart above the sensitivity limits of the Pan-STARRS/WISE data. But equally these may be asymmetric sources where the flux-weighted source position does not accurately coincide with the optical counterpart location or these sources may have clear substructure where one of the Gaussian components may coincide with the optical counterpart. Alternatively, these may be blended sources. To assess these possibilities, we again considered whether, and how many, Gaussian components have acceptable LR matches. In the case where no Gaussian components have LR matches (branch vii), it is very likely that the source of interest has no optical/IR identification. However, we also consider cases where the source may be complex or a component of a larger structure. Thus, sources whose Gaussian components are widely separated (maximum separation larger than $15''$) or sources that have an extended ($>10''$) neighbouring radio source within $100''$ were included in the LGZ sample. This is the only step where the decision differs significantly for the isolated and non-isolated “M” sources, where, by definition, a much higher fraction of non-isolated sources would be included in the LGZ sample. A visual sorting step was done on the non-isolated sources selected for LGZ, to avoid adding too many trivial sources with no optical/IR identification (again for clarity this is not shown explicitly in Fig. 6).

If only one Gaussian component has an acceptable LR match (branch viii) it was taken as the source match, provided it was deemed a good match ($LR_{\text{gauss}} > 10LR_{\text{thresh}}$ and the Gaussian size is $<10''$); these limits were again determined by visual inspection of subsamples of sources, in that a lower LR threshold or larger size threshold produced too many wrong matches while everything satisfying these criteria appeared to be genuine. Otherwise, the source was included in the LGZ sample.

Where there were two Gaussian components with acceptable LR matches (branch ix), if these matched to the same optical galaxy the source was handled in LGZ; this is because the lack of a good source LR match on this branch, combined with the two acceptable Gaussian LR matches, while likely to be the correct match, suggests some complex structure may be present. Otherwise if there were two separate optical galaxies, there is a strong possibility that the components were mistakenly grouped as a single source by PyBDSF and so the PyBDSF source was examined in the deblending workflow. Finally, the few sources with three or more Gaussian components with good LR matches were processed in LGZ (branch x).

7. Final catalogue

A final catalogue of LoTSS radio sources cross-matched to Pan-STARRS/WISE was produced by combining the identifications (and associations) from all the identification methods, including the LR method, LGZ, the deblending workflow, and the large galaxies. In the following, associated sources refer to those where separate PyBDSF sources have been associated and combined into single new sources either based on the LGZ output or matches with large optical galaxies (see Sect. 6.2). The individual PyBDSF sources that make up associated sources were removed from the catalogue and replaced with the associated sources. All artefacts, identified at various stages of the decision tree and LGZ, were removed from the catalogue (and also flagged as such in the catalogue of DR1-I). Sources that were identified as blends and processed in the deblending workflow were also removed and replaced by sources made up of one or more Gaussian components (see Sect. 5.4); they therefore have properties appropriate for associated sources in the catalogue. For all associated sources, we generated the LoTSS source properties and populated the appropriate final catalogue columns (e.g. total flux density, size, radio position, and radio source name) by combining the PyBDSF properties of their constituent components (or Gaussian components in the case of blends) as described in Sect. 5.3.

The LoTSS-DR1 value-added catalogue lists the radio properties, identification methods, and optical properties where available. The columns in the catalogue describing the LoTSS properties are as follows (for more details see DR1-I):

- The IAU source identification (“Source_Name”) based on the position of each source.
- LoTSS position and errors (“RA”, “E_RA”, “Dec”, and “E_Dec”). In the case of associated sources, this is the flux-weighted mean of the component values.
- LoTSS peak and total flux densities and associated errors (“Peak_flux”, “E_Peak_flux”, “Total_flux”, and “E_Total_flux”). In the case of associated sources this is the maximum of the peak flux densities and sum of the total flux densities of the components.
- LoTSS shape (“Maj”, “E_Maj”, “Min”, “E_Min”, “PA”, “E_PA”) and deconvolved shape (“DC_Maj”, “E_DC_Maj”, “DC_Min”, “E_DC_Min”, “DC_PA”, “E_DC_PA”). Deconvolved values are zero for unresolved sources. All these values are blank for associated sources whose shapes are described in different columns outlined below.
- Local rms noise in the LoTSS map (“Isl_rms”). In the case of associated sources this is the mean value of the components.
- Multiple Gaussian code (“S_Code”) is “M” in the case where the source consists of multiple Gaussian components or associated sources, “S” where it consists of a single Gaussian, and “C” in the case where the source lies within the same

island as another source. These codes are updated for the sources that are associated or deblended.

- Name of the LoTSS mosaic in which the source can be found (“Mosaic_ID”).
- The ratio of the number of LoTSS pointings in which the source is in the CLEAN mask to the number of pointings which are mosaicked at the position of the source (“Masked_Fraction”).

The associated sources have values for the following additional columns for their LoTSS properties determined as described in Sect. 5.3 (these are blank for non-associated sources):

- Shape measurements for associated sources (“LGZ_Size”, “LGZ_Width”, “LGZ_PA”).
- The number of PyBDSF sources in the association (“LGZ_Assoc”).
- A quality flag for the association (“LGZ_Assoc_Qual”). For LGZ this is the fraction of all views of this source region for which the listed association was chosen as the best associated set. Only sets with LGZ_Assoc_Qual > 2/3, and, of those, only the largest set for each LGZ input source are included in the final catalogue, with a small number of overlapping association sets resolved visually (see Sect. 5.2). This flag is set to 1 for the sources automatically associated based on a bright galaxy match or in the deblending workflow.

Information pertaining to the optical/IR identification is given by the following:

- A flag indicating the origin of the optical/IR identification or non-identification (“ID_flag”). The description of these flags can be found in Table 4. For ID_flag = 0, no attempt is made at an identification, while for the other values, the ID_flag indicates only which method was used to attempt an identification and not whether an ID is made. For example, a source with ID_flag = 1 may have an optical/IR identification above the LR threshold or it may have no acceptable LR identification.
- Name (“ID_name”) and position (“ID_RA” and “ID_Dec”) of the optical/IR identification, when present (sources with no identification can be recognised because they have no ID_name, ID_ra and ID_dec values). The recorded values are the Pan-STARRS object name and position or the AllWISE source name and position in the case of no Pan-STARRS detection. A small number (1078) of sources with a match to a bright galaxy (either through the decision tree or LGZ “host broken up”) have an ID_name from 2MASX or SDSS, while the position is taken from the nearest match for that 2MASX or SDSS source in the merged Pan-STARRS/AllWISE catalogue, with the caveat that the PanSTARRS and AllWISE photometry is likely to be wrong for these large sources.
- The LR for sources where the identification is made through this maximum likelihood method (“ML_LR”).
- A quality flag for LGZ identifications (“LGZ_ID_Qual”). This is set to the fraction of all LGZ views of this source region for which the catalogued ID was selected. Only IDs with LGZ_ID_Qual > 2/3, and only the highest quality ID for each source, were included in the catalogue.
- For deblended sources, the name of the PyBDSF multiple Gaussian component source from which each source was deblended (“Deblended_from”). This is blank for all other sources.

For the sources that have optical/IR identifications, we include the Pan-STARRS and AllWISE photometry:

- The name of the source in the AllWISE catalogue, “AllWISE”.

Table 4. Descriptions of the ID_flag keyword in the final catalogues used to indicate the origin of the possible association and optical/IR identification, or lack thereof.

ID_flag	Description
0	No identification is possible – in cases of extended diffuse emission
1	The identification (or lack thereof) is made through the LR method
2	The identification, and possible association, is made based on a match to a bright optical/IR galaxy
22	The identification is made based on a match to a bright optical/IR galaxy after classification, and possible association, in LGZ as “host broken up”
31	The possible association and identification (or lack thereof) is made through LGZ
32	The possible association and identification (or lack thereof) is made after further processing when classified as “too zoomed in” in LGZ (on branch B of the decision tree)
41	The source and identification (or lack thereof) comes from the deblending workflow based on the “M” source decision tree
42	The source and identification (or lack thereof) comes from the deblending workflow after classification in LGZ as “blend”

- The Pan-STARRS object ID, “objID”.
- Pan-STARRS forced aperture fluxes, magnitudes, and errors in the Pan-STARRS *grizy* bands (“<band>FapFlux”, “<band>FapFluxErr”, “<band>FapMag”, and “<band>FapMagErr”).
- Pan-STARRS Kron fluxes and errors in the Pan-STARRS *grizy* bands (“<band>FKronFlux” and “<band>FKronFluxErr”).
- AllWISE profile fitted fluxes, magnitudes, and errors in the WISE W1, W2, W3, and W4 bands (“<band>Flux”, “<band>FluxErr”, “<band>Mag”, and “<band>MagErr”). Sources with zero “Flux” values in a particular band were not detected in that band, and they have a 1σ upper limit given in the “FluxErr” column.

Additional columns pertaining to the photometric redshifts and rest-frame colours are described by [DR1-I](#).

We also retain a component catalogue of the sources in the PyBDSF catalogue associated as components in the final LoTSS-DR1 value-added catalogue. Each entry in the component catalogue has an identifier “Component_Name” based on the component position in the PyBDSF catalogue and a “Source_Name”, which corresponds to that in the value-added catalogue. The component catalogue includes a column, “Ng”, that gives the number of Gaussian components in each source. It also includes the additional CLEAN mask columns, “Number_Masked”, and “Number_Pointings”, giving the number of LoTSS pointings in which the source is in the CLEAN mask and the number of pointings which are mosaicked at the position of the source (see [DR1-I](#)). Each deblended source also appears as a component in the components catalogue; for these sources, we include the column, “Deblended_from”, which gives the name of the PyBDSF multiple Gaussian component source from which each source was deblended.

The catalogues presented in this paper are now publicly available¹⁴. The final catalogue contains 318 520 radio sources, of which 231 716 (73%) have optical/IR identifications. Table 5 shows the total number of sources, as well as the number and fraction of sources with an identification, for the different identification methods. The majority of the identifications come from the LR method with an overall identification rate of 74%. The overall identification rate for the LGZ method is 60%. Sources identified on the basis of a bright optical galaxy have 100%

Table 5. Total number of sources and the number with identifications for each method of identification.

	Number	Number with ID	ID fraction
All Sources	318 520	231 716	0.73
LR	299 730	221 269	0.74
LGZ	11 989	7144	0.60
Deblending	2435	2338	0.96
Bright galaxy	965	965	1.00
No ID possible	3401	0	0.00

identifications by construction. The deblending route has a high identification rate as sources are generally only selected for deblending when there are clear optical/IR identifications for several of the components.

The number of sources and identification fractions for the LR and LGZ methods are shown as a function of flux density in Fig. 7. The identification fraction here is the ratio of the number of sources with identifications to the number of sources in that category, and therefore shows the variation in identification rate as a function of flux density for each method. Errors on the numbers and fractions, within each flux density bin, were estimated using Monte Carlo simulations drawn from Poissonian distributions; for large numbers this converges to the Gaussian distribution. The LGZ identification fraction drops from 75% for sources with flux densities above 100 mJy down to below 25% at the lowest flux densities. The decrease in LGZ identification at low flux densities can be explained by the fact that by construction the sources selected for LGZ processing are resolved and those at lower flux densities are more likely to be AGN at high redshifts whose host galaxies fall below the optical/IR flux limits of Pan-STARRS/AllWISE.

Figure 8 shows the relative contribution by the two main identification methods to the overall identification fraction for all sources as a function of 150-MHz flux density, i.e. the ratio of the number of sources with identifications within each category to the total number of sources. This shows the contribution of each identification method to the total identification rate as a function of flux density, highlighting the fact that the majority of the optical/IR identifications for radio sources above a few tens of mJy come from LGZ, while those for fainter sources come from the LR method. Interestingly, the overall identification fraction drops with decreasing flux density down to ≈ 5 mJy,

¹⁴ The LoTSS-DR1 images and catalogues, including the value-added catalogue presented here, can be found at <https://lofar-surveys.org>.

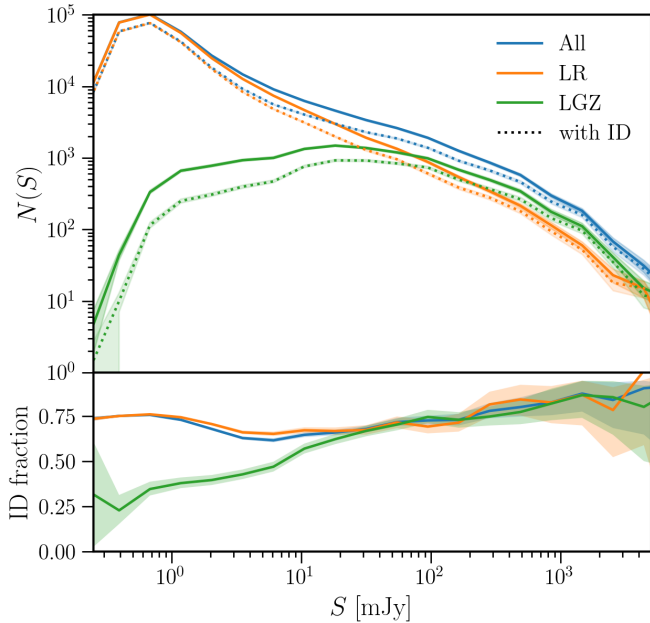


Fig. 7. Total number of sources (solid lines) and number of sources with identifications (dotted lines) as a function of 150-MHz flux density, in bins of 0.23 dex, for all sources (blue) and via the two major methods: LGZ (green) and LR (orange). The respective fractions of identifications (i.e. the ratio of the number of sources with identifications in each category to the number of sources in each category) as a function of flux density are shown in the bottom panel. Filled regions show the errors that are estimated using Monte Carlo simulations drawn from Poissonian distributions.

but then rises again at lower flux densities. These properties can be easily understood by considering the different radio source populations at different flux densities. At the brightest flux densities, the radio source counts are dominated by powerful radio-loud AGN, which often have extended complex radio structures requiring LGZ analysis. As the flux density decreases, the average redshift of these radio-loud AGN increases, leading to more of the optical counterparts falling below the magnitude limit of the Pan-STARRS and WISE catalogues and a decreasing overall ID fraction. At flux densities below a few mJy, however, the dominant contribution to the overall radio population switches: star-forming galaxies begin to dominate the radio source counts (e.g. Wilman et al. 2008; Padovani 2016; Williams et al. 2016). These are mostly at lower redshift, with consequently brighter counterparts, and are largely single radio components matching the counterpart position; this leads to an increasing proportion of the overall population for which IDs are found with most of these IDs coming from LRs.

8. Summary and future prospects

In this paper we have presented a catalogue of optical/IR identifications for radio sources in the first LoTSS data release presented by Shimwell et al. (2019; DR1-I). We have used a statistical colour- and magnitude-dependent LR method for the cross-matching of the majority of sources, complemented by LOFAR Galaxy Zoo (LGZ), a Zooniverse-based visual association and identification project, for sources with complex structure. The LGZ method, while time consuming, is well suited both for characterising large radio sources as well as identifying their optical/IR counterparts. The LR method cannot be used for such sources, but is an efficient way to identify the likely hosts

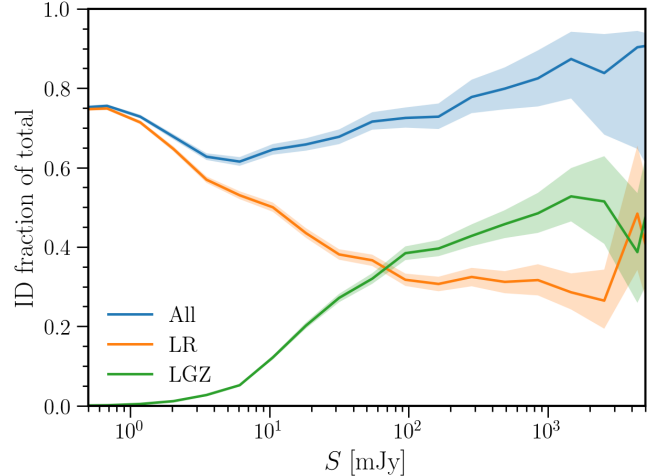


Fig. 8. Contribution to the overall identification fraction (i.e. the ratio of the number of sources with identifications within each category to the total number of sources) for sources at a given 150 MHz flux density, in bins of 0.23 dex, for all sources (blue) and via the two major methods: LGZ (green) and LR (orange). Filled regions show the errors that are estimated using Monte Carlo simulations drawn from Poissonian distributions.

of the majority of the LoTSS radio sources. We have therefore made use of a decision tree, based on the radio source properties and LRs, to select complex sources for visual classification with LGZ. This approach, of reserving the complex sources for visual classification while using statistical methods for the majority of sources, may be useful for future wide-area radio surveys.

The final radio source catalogue contains 318 520 entries, of which 231 716 (73%) have optical/IR identifications from Pan-STARRS and/or WISE (or in a few cases, 2MASX or SDSS). Most of the identifications at the brighter radio flux densities come from LGZ, while those at lower flux densities come from LR. In both cases, the identification rates depend on the quality and depth of the multiwavelength data and the underlying radio source population.

At just over 400 square degrees, LoTSS-DR1 covers only about 2% of the total sky area expected to be covered by LoTSS. Additionally, the LOFAR surveys will include deeper tiers covering smaller areas. Fortunately, the source population at fainter flux densities mostly comprises star-forming galaxies or faint unresolved AGN, which are well suited for cross-matching using the LR method (although a small number require deblending). The large increase in source numbers, in particular of the complex sources, within the full LoTSS coverage will require a different approach. This may involve an expansion of our LGZ Zooniverse project to the public, similar to “Radio Galaxy Zoo” (Banfield et al. 2015), which is using citizen scientists to cross-match over 170 000 radio sources. Work has been done on automated algorithms that can perform the cross-matching of complex radio sources (e.g. Proctor 2006; van Velzen et al. 2015; Fan et al. 2015), but these have mostly used simple pattern recognition algorithms that will only identify the simplest, most common, cases (e.g. well-defined double or triple sources). More recent work involves machine learning techniques such as self-organising maps or Kohonen maps (e.g. parallelised rotation/flipping INvariant Kohonen maps, or PINK; Polsterer et al. 2015) to construct prototypes of radio galaxy morphologies, which are being applied to the LoTSS data (Mostert 2017). Aniyani & Thorat (2017) have used convolutional neural networks to classify radio galaxy images into Fanaroff & Riley (1974) Type 1 or 2 (FRI/FRII)

classes. Similarly, Lukic et al. (2018) have classified radio galaxy morphologies in distinct classes, optimising the convolutional neural network parameters to produce four classes consisting of compact, single-, double-, and multiple-component extended sources. While many of these efforts are still focussed on the morphological classification of the radio structures and not on the optical/IR identification, they do allow a means to identify similar cases where the identification can be made relatively easily with automated algorithms, and outliers which may require human intervention to identify any counterparts.

The value of these identifications are further enhanced by estimates of the distances (via redshifts), from which one can calculate intrinsic properties such as luminosities and physical sizes. Photometric redshift and rest-frame colour estimates for all radio sources with identified optical counterparts presented in this paper are provided by Duncan et al. (2019; DR1-III). In the future, spectroscopic surveys such as WEAVE-LOFAR (Smith et al. 2016) will provide precise redshift estimates and robust source classification for large numbers of the LoTSS source population.

Acknowledgements. This paper is based on data obtained with the International LOFAR Telescope (ILT) under project codes LC2_038 and LC3_008. LOFAR (van Haarlem et al. 2013) is the LOw Frequency ARray designed and constructed by ASTRON. It has observing, data processing, and data storage facilities in several countries, which are owned by various parties (each with their own funding sources) and are collectively operated by the ILT foundation under a joint scientific policy. The ILT resources have benefited from the following recent major funding sources: CNRS-INSU, Observatoire de Paris and Université d'Orléans, France; BMBF, MIWF-NRW, MPG, Germany; Science Foundation Ireland (SFI), Department of Business, Enterprise and Innovation (DBEI), Ireland; NWO, The Netherlands; The Science and Technology Facilities Council, UK[7]. Part of this work was carried out on the Dutch national e-infrastructure with the support of SURF Cooperative through grant e-infra 160022 and we gratefully acknowledge support by N. Danezi (SURF-sara) and C. Schrijvers (SURFsara). This research has made use of the University of Hertfordshire high-performance computing facility (<http://uhhpc.herts.ac.uk/>) and the LOFAR-UK computing facility located at the University of Hertfordshire and supported by STFC [ST/P000096/1]. This research made use of ASTROPY, a community-developed core PYTHON package for astronomy (Astropy Collaboration 2013) hosted at <http://www.astropy.org/>, of APLPY (Robitaille & Bressert 2012), an open-source astronomical plotting package for PYTHON hosted at <http://aplpy.github.com/>, and of TOPCAT (Taylor 2005). The Pan-STARRS1 Surveys (PS1) and the PS1 public science archive have been made possible through contributions by the Institute for Astronomy, the University of Hawaii, the Pan-STARRS Project Office, the Max-Planck Society and its participating institutes, the Max Planck Institute for Astronomy, Heidelberg and the Max Planck Institute for Extraterrestrial Physics, Garching, the Johns Hopkins University, Durham University, the University of Edinburgh, the Queen's University Belfast, the Harvard-Smithsonian Center for Astrophysics, the Las Cumbres Observatory Global Telescope Network Incorporated, the National Central University of Taiwan, the Space Telescope Science Institute, the National Aeronautics and Space Administration under Grant No. NNX08AR22G issued through the Planetary Science Division of the NASA Science Mission Directorate, the National Science Foundation Grant No. AST-1238877, the University of Maryland, Eotvos Lorand University (ELTE), the Los Alamos National Laboratory, and the Gordon and Betty Moore Foundation. AllWISE makes use of data from WISE, which is a joint project of the University of California, Los Angeles, and the Jet Propulsion Laboratory/California Institute of Technology, and NEOWISE, which is a project of the Jet Propulsion Laboratory/California Institute of Technology. WISE and NEOWISE are funded by the National Aeronautics and Space Administration. This publication uses data generated via the Zooniverse.org platform, development of which is funded by generous support, including a Global Impact Award from Google, and by a grant from the Alfred P. Sloan Foundation. LW and MJH acknowledge support from the UK Science and Technology Facilities Council (STFC) under grant ST/M001008/1. PNB and JS are grateful for support from the UK STFC via grant ST/M001229/1. JHC and BM acknowledge support from the UK STFC under grants ST/M001326/1 and ST/R00109X/1. RKC, CLH, and RK acknowledge support from STFC studentships. VHM thanks the University of Hertfordshire for a research studentship [ST/N504105/1]. LA acknowledges support from the STFC through a ScotDIST Intensive Data Science Scholarship. GJW gratefully acknowledges support from the Leverhulme Trust. LKM acknowledges the

support of the Oxford Hinzte Centre for Astrophysical Surveys, which is funded through generous support from the Hintze Family Charitable Foundation. This publication arises from research partly funded by the John Fell Oxford University Press (OUP) Research Fund. GGU acknowledges support from the CSIRO OCE Postdoctoral Fellowship. The LOFAR group at Leiden acknowledges support from the ERC Advanced Investigator programme NewClusters 321271. RJvW further acknowledges support from the VIDI research programme with project number 639.042.729, which is financed by the Netherlands Organisation for Scientific Research (NWO). FdG is supported by the VENI research programme with project number 1808, which is financed by the NWO. APM would like to acknowledge support from the NWO/DOME/IBM programme "Big Bang Big Data: Innovating ICT as a Driver For Astronomy", project #628.002.001. AG acknowledges full support from the Polish National Science Centre (NCN) through the grant 2012/04/A/ST9/00083. MKB acknowledges support from the Polish National Science Centre under grant no. 2017/26/E/ST9/00216. IP acknowledges support from INAF under PRIN SKA/CTA "FORECaST".

References

- Alam, S., Albareti, F. D., Allende Prieto, C., et al. 2015, *ApJS*, **219**, 12
- Amendola, L., Appleby, S., Avgoustidis, A., et al. 2018, *Liv. Rev. Relat.*, **21**, 2
- Aniyan, A. K., & Thorat, K. 2017, *ApJS*, **230**, 20
- Astropy Collaboration (Robitaille, T. P., et al.) 2013, *A&A*, **558**, A33
- Banfield, J. K., Wong, O. I., Willett, K. W., et al. 2015, *MNRAS*, **453**, 2326
- Becker, R. H., White, R. L., & Helfand, D. J. 1995, *ApJ*, **450**, 559
- Best, P. N. 2004, *MNRAS*, **351**, 70
- Best, P. N., & Heckman, T. M. 2012, *MNRAS*, **421**, 1569
- Best, P. N., Arts, J. N., Röttgering, H. J. A., et al. 2003, *MNRAS*, **346**, 627
- Best, P. N., Kauffmann, G., Heckman, T. M., & Ivezić, Ž. 2005a, *MNRAS*, **362**, 9
- Best, P. N., Kauffmann, G., Heckman, T. M., et al. 2005b, *MNRAS*, **362**, 25
- Chambers, K. C., Magnier, E. A., Metcalfe, N., et al. 2016, *ArXiv e-prints* [arXiv:1612.05560]
- Cileigi, P., Zamorani, G., Hasinger, G., et al. 2003, *A&A*, **398**, 901
- Condon, J. J. 1997, *PASP*, **109**, 166
- Condon, J. J., Cotton, W. D., Greisen, E. W., et al. 1998, *AJ*, **115**, 1693
- Cutri, R. M., Strutskie, M. F., van Dyk, S., et al. 2013, *VizieR Online Data Catalog*: II/328
- Dalton, G., Trager, S. C., Abrams, D. C., et al. 2012, in *Ground-based and Airborne Instrumentation for Astronomy IV*, *Proc. SPIE*, **8446**, 84460P
- Dalton, G., Trager, S., Abrams, D. C., et al. 2014, in *Ground-based and Airborne Instrumentation for Astronomy V*, *Proc. SPIE*, **9147**, 91470L
- de Ruiter, H. R., Willis, A. G., & Arp, H. C. 1977, *A&A*, **28**, 211
- Duncan, K. J., Sabater, J., Röttgering, H. J. A., et al. 2019, *A&A*, **622**, A3 (LOFAR SI)
- Fan, D., Budavári, T., Norris, R. P., & Hopkins, A. M. 2015, *MNRAS*, **451**, 1299
- Fanaroff, B. L., & Riley, J. M. 1974, *MNRAS*, **167**, 31P
- Fleuren, S., Sutherland, W., Dunne, L., et al. 2012, *MNRAS*, **423**, 2407
- Hardcastle, M. J., Gürkan, G., van Weeren, R. J., et al. 2016, *MNRAS*, **462**, 1910
- Hill, G. J., & Lilly, S. J. 1991, *ApJ*, **367**, 1
- Hill, G. J., Gebhardt, K., Komatsu, E., et al. 2008, *Evol.*, **399**, 115
- Huynh, M. T., Jackson, C. A., Norris, R. P., & Prandoni, I. 2005, *AJ*, **130**, 1373
- Ivezić, V., Tyson, J. A., Acosta, E., et al. 2008, *ArXiv e-prints* [arXiv:0805.2366v4]
- Janssen, R. M. J., Röttgering, H. J. A., Best, P. N., & Brinchmann, J. 2012, *A&A*, **541**, A62
- Jarrett, T. H., Chester, T., Cutri, R., et al. 2000, *AJ*, **119**, 2498
- Johnston, S., Bailes, M., Bartel, N., et al. 2007, *PASA*, **24**, 174
- Jones, D. H., Saunders, W., Colless, M., et al. 2004, *MNRAS*, **355**, 747
- Kaiser, N., Aussel, H., Burke, B. E., et al. 2002, in *Survey and Other Telescope Technologies and Discoveries*, eds. J. A. Tyson, et al., *Proc. SPIE*, **4836**, 154
- Kaiser, N., Burgett, W., Chambers, K., et al. 2010, in *Ground-based and Airborne Telescopes III*, *Proc. SPIE*, **7733**, 77330E
- Lintott, C. J., Schawinski, K., Slosar, A., et al. 2008, *MNRAS*, **389**, 1179
- Lukic, V., Brüggen, M., Banfield, J. K., et al. 2018, *MNRAS*, **476**, 246
- Mauch, T., & Sadler, E. M. 2007, *MNRAS*, **375**, 931
- McAlpine, K., Smith, D. J. B., Jarvis, M. J., Bonfield, D. G., & Fleuren, S. 2012, *MNRAS*, **423**, 132
- Merloni, A., Predehl, P., Becker, W., et al. 2012, *ArXiv e-prints* [arXiv:1209.3114]
- Mohan, N., & Rafferty, D. 2015, *Astrophysics Source Code Library* [record ascl:1502.007]
- Mostert, R. I. J. 2017, Master's Thesis, Leiden University, The Netherlands
- Nisbet, D. M. 2018, PhD Thesis, The University of Edinburgh, UK
- Norris, R. P., Hopkins, A. M., Afonso, J., et al. 2011, *PASA*, **28**, 215
- Oke, J. B., & Gunn, J. E. 1983, *ApJ*, **266**, 713
- Padovani, P. 2016, *A&ARv*, **24**, 13

- Polsterer, K. L., Gieseke, F., & Igel, C. 2015, in *Astronomical Data Analysis Software and Systems XXIV (ADASS XXIV)*, eds. A. R. Taylor, & E. Rosolowsky, *ASP Conf. Ser.*, 495, 81
- Prandoni, I., Gregorini, L., Parma, P., et al. 2000, *A&A*, 146, 41
- Prestage, R. M., & Peacock, J. A. 1988, *MNRAS*, 230, 131
- Proctor, D. D. 2006, *ApJS*, 165, 95
- Rengelink, R. B., Tang, Y., de Bruyn, A. G., et al. 1997, *A&A*, 124, 259
- Richter, G. A. 1975, *Astron. Nachr.*, 296, 65
- Robitaille, T., & Bressert, E. 2012, *Astrophysics Source Code Library* [record ascl:1208.017]
- Röttgering, H., Afonso, J., Barthel, P., et al. 2011, *JApA*, 32, 557
- Schlegel, D. J., Finkbeiner, D. P., & Davis, M. 1998, *ApJ*, 500, 525
- Shimwell, T. W., Röttgering, H. J. A., Best, P. N., et al. 2017, *A&A*, 598, A104
- Shimwell, T. W., Tasse, C., Hardcastle, M. J., et al. 2019, *A&A*, 622, A1 (LOFAR SI)
- Skrutskie, M. F., Cutri, R. M., Stiening, R., et al. 2006, *AJ*, 131, 1163
- Smith, D. J. B., Best, P. N., Duncan, K. J., et al. 2016, in *SF2A-2016: Proceedings of the Annual meeting of the French Society of Astronomy and Astrophysics*, eds. C. Reylé, J. Richard, L. Cambrésy, et al., 271
- Stoughton, C., Lupton, R. H., Bernardi, M., et al. 2002, *AJ*, 123, 485
- Sutherland, W., & Saunders, W. 1992, *MNRAS*, 259, 413
- Taylor, M. B. 2005, in *Astronomical Data Analysis Software and Systems XIV*, eds. P. Shopbell, M. Britton, & R. Ebert, *ASP Conf. Ser.*, 347, 29
- van Haarlem, M. P., Wise, M. W., Gunst, A. W., et al. 2013, *A&A*, 556, A2
- van Velzen, S., Falcke, H., & Körding, E. 2015, *MNRAS*, 446, 2985
- Verheijen, M. A. W., Oosterloo, T. A., van Cappellen, W. A., et al. 2008, in *The Evolution of Galaxies Through the Neutral Hydrogen Window*, eds. R. Minchin, & E. Momjian, *AIP Conf. Ser.*, 1035, 265
- Williams, W. L., van Weeren, R. J., Röttgering, H. J. A., et al. 2016, *MNRAS*, 460, 2385
- Wilman, R. J., Miller, L., Jarvis, M. J., et al. 2008, *MNRAS*, 388, 1335
- Wright, E. L., Eisenhardt, P. R. M., Mainzer, A. K., et al. 2010, *AJ*, 140, 1868
- York, D. G., Adelman, J., Anderson, Jr., J. E., et al. 2000, *AJ*, 120, 1579
- ² SUPA, Institute for Astronomy, Royal Observatory, Blackford Hill, Edinburgh EH9 3HJ, UK
- ³ School of Physical Sciences, The Open University, Walton Hall, Milton Keynes MK7 6AA, UK
- ⁴ Leiden Observatory, Leiden University, PO Box 9513, 2300 RA Leiden, The Netherlands
- ⁵ ASTRON, The Netherlands Institute for Radio Astronomy, Postbus 2, 7990 AA Dwingeloo, The Netherlands
- ⁶ CSIRO Astronomy and Space Science, PO Box 1130, Bentley, WA 6102, Australia
- ⁷ Astronomical Observatory, Jagiellonian University, ul. Orla 171, 30-244 Kraków, Poland
- ⁸ Astrophysics, University of Oxford, Denys Wilkinson Building, Keble Road, Oxford OX1 3RH, UK
- ⁹ Jodrell Bank Centre for Astrophysics, School of Physics and Astronomy, University of Manchester, Manchester M13 9PL, UK
- ¹⁰ Toruń Centre for Astronomy, Faculty of Physics, Astronomy and Informatics, NCU, Grudziacka 5, 87-100 Toruń, Poland
- ¹¹ INAF – Istituto di Radioastronomia, Via Gobetti 101, 40129 Bologna, Italy
- ¹² Anton Pannekoek Institute for Astronomy, University of Amsterdam, Postbus 94249, 1090 GE Amsterdam, The Netherlands
- ¹³ GEPI, Observatoire de Paris, CNRS, Université Paris Diderot, 5 place Jules Janssen, 92190 Meudon, France
- ¹⁴ Department of Physics & Electronics, Rhodes University, PO Box 94, Grahamstown 6140, South Africa
- ¹⁵ Space Science & Technology Department, The Rutherford Appleton Laboratory, Chilton, Didcot, Oxfordshire OX11 0NL, UK
- ¹⁶ University of Hamburg, Hamburger Sternwarte, Gojenbergsweg 112, 21029 Hamburg, Germany
- ¹⁷ Thüringer Landessternwarte (TLS), Sternwarte 5, 07778 Tautenburg, Germany
- ¹⁸ Kapteyn Astronomical Institute, PO Box 800, 9700 AV Groningen, The Netherlands
- ¹⁹ Fakultät für Physik, Universität Bielefeld, Postfach 100131, 33501 Bielefeld, Germany

¹ Centre for Astrophysics Research, School of Physics, Astronomy and Mathematics, University of Hertfordshire, College Lane, Hatfield AL10 9AB, UK
e-mail: wwilliams@strw.leidenuniv.nl